Heterogeneous Kinetics of H_2O, HNO_3 and HCl on HNO_3 hydrates (α-NAT, β-NAT, NAD) in the range 175-200 K

Riccardo Iannarelli[1,2] and Michel J. Rossi[1]

[1]Laboratory of Atmospheric Chemistry (LAC), Paul Scherrer Institute (PSI), CH-5232 PSI Villigen, Switzerland; [2]New address: Safety, Prevention and Health Domain, RI DSPS-SCC , Station 6, Ecole Polytechnique Fédérale de Lausanne (EPFL), CH-1015 Ecublens, Switzerland.

Correspondence to: M. J. Rossi (michel.rossi@psi.ch)

Abstract

Experiments on the title compounds have been performed using a multidiagnostic stirred-flow reactor (SFR) in which the gas- as well as the condensed phase has been simultaneously investigated under stratospheric temperatures in the range 175-200 K. Wall interactions of the title compounds have been taken into account using Langmuir adsorption isotherms in order to close the mass balance between deposited and desorbed (recovered) compounds. Thin solid films at 1 μm typical thickness have been used as a proxy for atmospheric ice particles and have been deposited on a Si window of the cryostat with the optical element being the only cold point in the deposition chamber. FTIR absorption spectroscopy in transmission as well as partial and total pressure measurement using residual gas MS and sensitive pressure gauges have been employed in order to monitor growth and evaporation processes as a function of temperature using both pulsed and continuous gas admission and monitoring under SFR conditions. Thin solid H_2O ice films were used as the starting point throughout, with the initial spontaneous formation of α-NAT followed by the gradual transformation of α-➔ β-NAT at T > 185 K. NAD was spontaneously formed at somewhat larger partial pressures of HNO_3 deposited on pure H_2O ice. In contrast to published reports the formation of α-NAT proceeded without prior formation of an amorphous HNO_3/H_2O layer and always resulted in β-NAT. For α- and β-NAT the temperature dependent accommodation coefficient $\alpha(H_2O)$ and $\alpha(HNO_3)$, the evaporation flux $J_{ev}(H_2O)$ and $J_{ev}(HNO_3)$ and the resulting saturation vapor pressure $P_{eq}(H_2O)$ and $P_{eq}(HNO_3)$ were measured and compared to binary phase diagrams of HNO_3/H_2O in order to afford thermochemical check of the kinetic parameters. The resulting

kinetic and thermodynamic parameters of activation energies for evaporation (E_{ev}) and standard heats of evaporation ΔH_{ev}^0 of H_2O and HNO_3 for α- and β-NAT, respectively, led to an estimate for the relative standard enthalpy difference between α- and β-NAT of -6.0 ± 20 kJ/mol in favor of β-NAT, as expected, despite a significantly larger value of E_{ev} for HNO_3 in α-NAT. This in turn implies a substantial activation energy for HNO_3 accommodation in α- compared to β-NAT where $E_{acc}(HNO_3)$ is essentially zero. The kinetic ($\alpha(HCl)$, $J_{ev}(HCl)$) and thermodynamic ($P_{eq}(HCl)$) parameters of HCl-doped α- and β-NAT have been determined under the assumption that HCl adsorption did not significantly affect $\alpha(H_2O)$ and $\alpha(HNO_3)$ as well as the evaporation flux $J_{ev}(H_2O)$. $J_{ev}(HCl)$ and $P_{eq}(HCl)$ on both α- and β-NAT are larger than the corresponding values for HNO_3 across the investigated temperature range but significantly smaller than the values for pure H_2O ice at T < 200 K.

1 Introduction

Heterogeneous processes taking place on ice clouds in the Upper Troposphere (UT) or on Polar Stratospheric Clouds (PSC's) in the Lower Stratosphere (LS) have, since a long time, been recognized as one of the major ozone depleting mechanism (Solomon et al., 1986). PSC's consist of either particles of crystalline nitric acid trihydrate (NAT) (type Ia), ternary $H_2SO_4/HNO_3/H_2O$ supercooled solutions (type Ib) or pure H_2O ice (type II) (Zondlo et al. 2000) and are formed during the polar winter season when temperatures are sufficiently low in order to allow H_2O supersaturation that ultimately leads to cloud formation in the dry stratosphere subsequent to ice nucleation (Peter, 1997).

Ozone is depleted during the Arctic and Antarctic spring season after unreactive chlorine reservoir compounds, $ClONO_2$ and HCl, are converted into molecular chlorine and rapidly photolyze into active atomic chlorine during the spring season (Solomon, 1990). The presence of PSC's enables heterogeneous chemical reactions such as Reaction (R1), which represents one of the most efficient stratospheric heterogeneous reactions (Friedl et al, 1986; Molina et al., 1985, 1987):

$$ClONO_2(g) + HCl(s) \rightarrow Cl_2(g) + HNO_3(s) \qquad (R1)$$

Reaction (R1) is orders of magnitude faster than the corresponding homogeneous gas phase process (Molina et al., 1985) and the most important chlorine-activating reactions in the polar stratosphere are reported in Reactions (R2)-(R4):

$$X + O_3 \rightarrow XO + O_2 \quad \text{(R2)}$$

$$\underline{XO + O \rightarrow X + O_2} \quad \text{(R3)}$$

$$\text{net: } O_3 + O \rightarrow O_2 + O_2 \quad \text{(R4)}$$

where X is H, OH, NO, Cl or Br leading to HO_x, NO_x, ClO_x and BrO_x catalytic cycles, respectively.

Reaction (R1) increases the concentration of HNO_3 in the condensed phase and when PSC particles become sufficiently large they fall out of the stratosphere (Fahey et al., 2001) which inhibits Reaction (R5):

$$ClO + NO_2 + M \rightarrow ClONO_2 + M \quad \text{(R5)}$$

and prevents formation of reservoir species with longer atmospheric residence times.

The study of HNO_3 interaction with ice in the temperature and pressure ranges typical of the UT/LS is crucial in order to understand the de-nitrification process initiated by reaction (R1) and its effectiveness in the overall ozone destruction mechanism. To this purpose, many research groups (Voigt et al., 2000, 2005; Fahey et al., 2001; Schreiner et al., 2003; Gao et al., 2004; Höpfner et al., 2006) have studied the composition of PSC's using both *in situ* and remote sensing techniques both in the Arctic as well as above Antarctica. A balloon borne experiment at first detected non-crystalline HNO_3 hydrates (Schreiner et al., 1999), later both balloon borne (Voigt et al., 2000; Schreiner et al., 2003) and aircraft campaigns (Voigt et al., 2005) obtained unambiguous proof of the presence of crystalline HNO_3 hydrates (NAT) at altitudes between 18 and 24 km in the Arctic. The presence of β-NAT, through the identification of type Ia PSC's, has been unambiguously confirmed by Höpfner et al. (2006) using the MIPAS instrument on a satellite platform by comparison of measured limb-emission spectra of polar stratospheric clouds with measured optical constants in the region of the symmetric NO_3 peak at $\nu_2 = 820$ cm^{-1}.

The existence of several crystalline hydrates of nitric acid has been confirmed for several years. Hanson and Mauersberger (1988) have identified two stable hydrates, namely, nitric acid monohydrate (NAM, $HNO_3 \bullet H_2O$) and nitric acid trihydrate (NAT, $HNO_3 \bullet 3H_2O$) the latter of which is thought to be of atmospheric importance. Several distinct crystalline hydrates of HNO_3 have been found by Ritzhaupt and Devlin (1991) in their work examining the infrared absorption spectrum of thin film samples. By depositing the equilibrium vapours

of aqueous HNO_3 solutions of different concentrations at 293 K they observed nitric acid dihydrate (NAD, $HNO_3 \bullet 2H_2O$), NAM and NAT. Ji and Petit have performed an extensive investigation on the thermochemical properties of NAD (Ji and Petit, 1993).

Tolbert and coworkers have also reported infrared absorption spectra of NAM, NAD and NAT in a series of studies. Tolbert and Middlebrook (1990) have co-condensed calibrated mixtures of H_2O/HNO_3 vapours onto a cryostat and assigned the absorption spectra of the growing thin films to nitric acid hydrates (NAM, NAD or NAT) according to the ratio of the dosing gases. Koehler et al. (1992) have observed the Fourier transform infrared (FTIR) absorption spectra in transmission of nitric acid hydrate thin films and measured their composition using temperature-programmed desorption (TPD). They confirmed the previously assigned spectra of NAD and NAM. They were also the first to observe two distinct structures of NAT: a low-temperature and metastable structure called α-NAT whose structure has recently been elucidated (Weiss et al., 2016) and a thermodynamically stable high-temperature structure named β-NAT. Middlebrook et al. (1992) observed that NAD consistently converts to β-NAT when exposed to H_2O partial pressures typical of the stratosphere and therefore proposed that NAD is also metastable under stratospheric conditions.

Several other groups have investigated the structure of nitric acid hydrates and published absorption spectra of both α-NAT and β-NAT in the mid-IR range, using grazing incidence Reflection Absorption IR spectroscopy (RAIRS) (Zondlo et al., 1998; Zondlo et al., 2000; Ortega et al., 2003; Ortega et al., 2006; Herrero et al., 2006; Escribano et al., 2007) and FTIR in transmission (Tso and Leu, 1996; Martin-Llorente et al., 2006; Ortega et al., 2006).

Compared to the molecular properties of the nitric acid hydrates knowledge of the kinetic parameters of trace gases interacting with HNO_3 hydrates is scarce. Middlebrook et al. (1992) have used time-dependent FTIR monitoring of the optical density of growing NAT films during deposition to measure the uptake of H_2O and HNO_3 on NAT. They reported a value of $\gamma_{NAT}(HNO_3) > 0.4$ for HNO_3 net uptake (γ) on NAT at T = 197 K whereas $2.0\times10^{-3} \leq \gamma_{NAT}(H_2O) \leq 1.0\times10^{-2}$ is reported for H_2O. The range measured for $\gamma_{NAT}(H_2O)$ corresponds to the HNO_3 pressure used during the deposition. Using evaporation experiments in a slow-flow reactor Biermann et al. (1998) measured the accommodation coefficient of H_2O on β-NAT substrates, $\alpha_{\beta-NAT}(H_2O)$, from the thickness of the substrate measured using FTIR

absorption. They found no temperature dependence, reporting lower limiting values of $\alpha_{\beta-NAT}(H_2O) = (2.2 – 6.0)\times10^{-2}$ in the range 192-202 K.

Delval and Rossi (2005) have used a multidiagnostic flow reactor, similar to the one used in this work, coupled with a quartz crystal microbalance (QCMB) for the measurement of the evaporation rate of H_2O from α-NAT and β-NAT thin films. They reported a positive temperature dependence of $\alpha_{\alpha-NAT}(H_2O)$ and a negative temperature dependence of $\alpha_{\beta-NAT}(H_2O)$ in the range 179-208 K.

Hanson (1992) also measured the uptake coefficient of HNO_3 on NAT using a cold coated-wall flow tube with HNO_3 deposited on ice condensed on the cold flow tube walls and reported $\gamma_{NAT}(HNO_3) > 0.3$. A rapid uptake was observed which decreased as the surface coverage or dose of HNO_3 increased. Furthermore, the observed steady state partial pressure of HNO_3 over the ice substrate is about a factor of 5 higher than the HNO_3 vapor pressure over NAT and thus indicates that no hydrate was actually formed during the experiments. Therefore, the observed uptake has most likely to be attributed to uptake on other cold surfaces in the flow reactor.

Reinhardt et al. (2003) reported $\gamma_{NAT}(HNO_3) = 0.165$ in the temperature range 160 to 170 K. They used a slow flow reaction cell coupled with DRIFTS (Diffuse Reflectance Infrared Fourier Transform Spectroscopy) for the detection of adsorbed species and downstream FTIR for the detection of gas phase HNO_3.

In the investigation of the properties of binary chemical systems the behavior of the simple single-component systems is an important stepping stone. Hynes et al. (2002) observed continuous uptake of HNO_3 on water-ice films below 215 K and time dependent uptake above 215 K, with the maximum uptake $\gamma_{ice}(HNO_3)$ decreasing from 0.03 at 215 K down to 0.006 at 235 K. They also observed that the uptake of HCl at 218 K on ice surfaces previously dosed with HNO_3 is reversible. Furthermore, the adsorption of HNO_3 on ice surfaces which contained previously adsorbed HCl indicates that HCl is displaced from surface sites by HNO_3.

In this work, the results for the kinetics of H_2O and HNO_3 gas interacting with spectroscopically characterized HNO_3 hydrates will be presented. The independent measurement of the absolute rate of evaporation R_{ev} [molec s^{-1} cm^{-3}] and the accommodation coefficient α of H_2O and HNO_3 on α- and β-NAT substrates is performed using a

combination of steady state and real-time pulsed valve experiments. Results on the kinetics of the ternary system HCl on HNO_3 hydrates will also be presented. All experiments reported in this work have been performed using a multidiagnostic stirred flow reactor (SFR) in the molecular flow regime, which has been described in detail before (Chiesa and Rossi, 2013; Iannarelli and Rossi, 2014). In addition, all experiments have been performed under strict mass balance control by considering how many molecules of HNO_3, HCl and H_2O were present in the gas vs. the condensed phase (including the vessel walls) at any given time. These experiments have been described by Iannarelli and Rossi (2015). Most importantly, the consistency of the accommodation and evaporation kinetics has been checked using the method of thermochemical kinetics (Benson, 1976) by calculating the equilibrium vapor pressure and comparing it with values of published phase diagrams. In addition, the present work is the first to present absolute rates of evaporation of all involved constituents (H_2O, HNO_3, HCl) thus enabling predictions on evaporative lifetimes of ice particles under atmospheric conditions.

2 Experimental Apparatus and Methodology

2.1 Experimental Apparatus and Growth Protocols

Figure 1 shows a diagram of the reactor used in this work with the experimental diagnostic tools and Table 1 reports its characteristic parameters. Briefly, it consists of a low-pressure stainless steel reactor, which may be used under static (all valves closed) or stirred flow (gate valve closed, leak valves open) conditions. We use absolute total pressure measurement and calibrated residual gas mass spectrometry (MS) to monitor the gas phase and FTIR spectroscopy in transmission for the condensed phase. Thin solid films of up to 2 μm thickness are grown on a temperature controlled Si substrate and an average of 8 scans are recorded at 4 cm^{-1} resolution in the spectral range 700-4000 cm^{-1} at typical total scan time of 45-60 s.

The 1” Si window is the only cold spot in the reactor exposed to admitted gases and therefore the only place where gas condensation occurs. This allows the establishment of a 1:1 correspondence between the thin film composition and the changes in the gas partial pressures in the reactor. Experimental proof of mass balance has previously been reported for this setup (Delval et al., 2003; Chiesa and Rossi, 2013; Iannarelli and Rossi, 2014; 2015).

185 The introduction of HNO_3 in the system forced us to slightly modify the inlet system used
186 previously (Iannarelli and Rossi, 2014) in order to take into account the fact that HNO_3 is an
187 extremely "sticky" molecule that interacts with the internal surfaces of the reservoir vessel of
188 the inlet system as well as with the reactor walls of the SFR (Iannarelli and Rossi, 2015). We
189 therefore minimized the volume of the admission system and only retained the absolutely
190 necessary total pressure gauge for measuring the absolute inlet flow rate (molecule s^{-1}).

191 Similarly to the case of HCl and H_2O (Iannarelli and Rossi, 2014) we have described the
192 HNO_3 interaction with the reactor walls using a Langmuir adsorption isotherm and
193 determined the concentration of HNO_3 in the ice sample after calibration of HNO_3 following
194 the methodology described in Iannarelli and Rossi (2015). Table 2 reports the values of the fit
195 parameters of the Langmuir adsorption isotherms for all the gases interacting with the
196 stainless steel (SS304) internal surfaces of the SFR. Binary combinations of HNO_3/H_2O and
197 HCl/H_2O have been used to describe the interaction of the acidic probe gas with the vessel
198 walls in the presence of H_2O vapor.

199 The protocol for the growth of α-NAT, β-NAT and NAD thin films has also been described
200 in Iannarelli and Rossi (2015). Briefly, the protocol for either hydrate always starts with the
201 growth of pure ice: the chamber is backfilled under SFR conditions with water vapor at flow
202 rates between 5×10^{15} and 10^{16} molec s^{-1}, corresponding to a partial pressure of H_2O, $p(H_2O)$
203 between 4.7 and 9.4×10^{-4} Torr (both apertures open), with the Si substrate held at temperature
204 in the range 167 to 175 K. The pure ice film grows on both sides of the Si substrate to a
205 thickness of typically 1 μm until the H_2O flow is halted (Iannarelli and Rossi, 2014). The
206 temperature of the support is then set to the value used for the growth of the desired HNO_3
207 hydrate at a typical rate of ±0.3 K min^{-1}.

208 The growth protocols for α-NAT and NAD are similar and start after the deposition of a pure
209 ice film: the temperature of the Si substrate is held in the range 180 to 185 K for α-NAT and
210 at 168 K for NAD. The sample is exposed for approximately 10 min at SFR conditions to
211 HNO_3 vapor at flow rates in the range 3 to 7×10^{14} molecule s^{-1} for α-NAT and 9×10^{14}
212 molecule s^{-1} for NAD. The typical total dose of HNO_3 admitted into the reactor is 2 to 3×10^{17}
213 molecules and 4×10^{17} molecules for α-NAT and NAD, respectively, with almost all of it
214 adsorbed onto the ice film. In both cases, we observe the formation of a new phase after
215 approximately 5 min of exposure as shown in the change of the FTIR absorption spectrum.
216 The present experimental conditions seem to show that no nucleation barrier is present for α-

NAT and NAD growth, in agreement with previous works (Hanson, 1992; Middlebrook et al., 1992; Biermann et al., 1998). In contrast, Zondlo et al. (2000) have shown that crystalline growth occurs via an intermediate stage of supercooled H_2O/HNO_3 liquid forming over ice. After exposure the temperature of the substrate is set to the desired value for the kinetic experiments on α-NAT or NAD as a substrate.

The protocol for the growth of β-NAT is different compared to NAD and α-NAT hydrates as it only starts after the growth of an α-NAT film. After the HNO_3 flow has been halted, the α-NAT/ice system is set to static conditions and the temperature increased to 195 K. During the temperature increase the α-NAT film converts to β-NAT as shown by means of FTIR spectroscopy (Koehler et al., 1992; Iannarelli and Rossi, 2015), and once the conversion is completed the temperature is set to the desired value to start the kinetic experiments using β-NAT as substrate. Typical growth protocols under mass balance control showing both the FTIR transmission as well as the corresponding MS signals of HNO_3 as a function of deposition time have been published previously (Iannarelli and Rossi, 2015).

In all samples used for this work, we never have a pure HNO_3 hydrate because we always operate under conditions of excess or comparable amounts of pure ice. Excess ice has been shown to have a stabilizing effect on both α-NAT and β-NAT (Weiss et al., 2016) and in all our experiments the presence of excess ice has been confirmed by FTIR spectra (Iannarelli and Rossi, 2015).

2.2 Experimental Methodology

The experimental methodology used in this work is an extension of the methodology reported in Iannarelli and Rossi (2014) where the combination of real-time pulsed valve and steady state experiments allowed the independent measurement of the rate of evaporation R_{ev} [molec s^{-1} cm^{-3}] and the accommodation coefficient α of HCl and H_2O on crystalline and amorphous HCl hydrates.

For each gas X (X = H_2O, HNO_3, HCl) admitted into the reactor in the presence of ice, the following flow balance equation holds at steady state:

$$F_{in}(X) + F_{des}(X) + F_{ev}(X) = F_{SS}(X) + F_{ads,w}(X) + F_{ads,ice}(X) \qquad (1)$$

All terms in Equation (1) are flow rates in molec s^{-1} with the terms from left to right corresponding to molecules admitted into the reactor (F_{in}), molecules desorbing from the

reactor walls (F_{des}), molecules evaporating from the ice surface (F_{ev}), molecules effusing through the leak valve into the MS chamber (F_{SS}), molecules adsorbing onto the reactor walls ($F_{ads,w}$) and molecules adsorbing onto the ice film ($F_{ads,ice}$).

Under the assumption that the adsorption onto the walls may be described as a Langmuir-type adsorption, Eq. (1) may be expressed as follows for a gas X:

$$V \cdot R_{in}(X) + N_{TOT} \cdot k_{des,w}(X) \cdot \theta + V \cdot R_{ev}(X) = \\ = V \cdot R_{SS}(X) + S_w \cdot \frac{\alpha_w(X) \cdot \bar{c}}{4}(1-\theta)\,[X]_{SS} + S_{film} \cdot \frac{\alpha_{film}(X) \cdot \bar{c}}{4}[X]_{SS} \qquad (2)$$

where V is the reactor volume in cm^3, $R_{in}(X)$ the rate of molecules X admitted into the chamber in molec·s^{-1}·cm^{-3}, N_{TOT} the total number of molecules X adsorbed on the reactor walls, $k_{des,w}(X)$ the desorption rate constant from the reactor walls in s^{-1}, θ the fractional surface coverage in terms of a molecular monolayer, $R_{ev}(X)$ the rate of evaporation of X from the ice in molec·s^{-1}·cm^{-3}, $R_{SS}(X)$ the rate of effusion through the leak valve in molec·s^{-1}·cm^{-3}, S_w and S_{film} the surfaces of the reactor walls and the thin film in cm^2, $\alpha_w(X)$ and $\alpha_{film}(X)$ the accommodation coefficients of X on the walls and on the thin film, $[X]_{SS}$ the concentration at steady state in molec cm^{-3} and $\bar{c}$ the mean thermal velocity of a molecule in cm·s^{-1}, respectively. The mathematical derivation of Eq. (2) may be found in Supplement B of Iannarelli and Rossi (2014).

Pulsed valve (PV) experiments and Langmuir adsorption isotherms have been used in order to measure $k_{des,w}(X)$ and $\alpha_w(X)$ (Iannarelli and Rossi, 2014), leaving only two unknown parameters in Eq. (2): $R_{ev}(X)$ and $\alpha_{film}(X)$. The Langmuir adsorption isotherms are shown in Figure S1 of Supplement A whereas the parameters for the best fit are reported in Table 2.

In the case of H_2O, once the selected substrate has been grown according to the protocol briefly described above, the film is set to a chosen temperature. After steady state conditions are established, a series of H_2O pulses are admitted into the reactor. The exponential decay of the MS signal at m/z 18 (k_d) is given by the sum of the measured k_{esc}, the adsorption rate constant on the walls (k_w) and the adsorption rate constant (k_c) onto the ice, namely $k_d = k_{esc} + k_w + k_c$, in the aftermath of a pulse. The accommodation coefficient $\alpha_{film}(H_2O)$ may then be calculated according to Eq. (3):

$$\alpha_{film}(H_2O) = \frac{k_c(H_2O)}{\omega(H_2O)} \qquad (3)$$

where $\omega(H_2O)$ is the calculated gas-surface collision frequency in s^{-1} and is reported in Table 1.

The steady state MS signal established before the pulse series represents the calibrated flow rate of molecules effusing through the leak valve, $F_{SS}(H_2O)$, in Eq. (1) and may be used to calculate the concentration at steady state $[X]_{SS}$ according to Eq. (4):

$$[X]_{SS} = \frac{F_{SS}(X)}{k_{esc}(X)V} \quad (4)$$

where $k_{esc}(X)$ is the effusion rate constant of gas X out of the reactor in s^{-1} (see Table 1). Finally, $[X]_{SS}$ is used to calculate $R_{ev}(X)$ using Eq. (2).

Subsequently, the film is set to a higher temperature, $F_{SS}(H_2O)$ is recorded and a series of H_2O pulses applied to the same ice sample. This experimental protocol has been repeated for each measured point in the temperature interval of interest.

Under the present experimental conditions, PV experiments of HNO_3 leading to transient supersaturation of HNO_3 are hampered by excessive pulse broadening, most probably owing to the strong adsorption of HNO_3 on ice and the stainless steel vessel walls that makes the observation and interpretation of a HNO_3 pulse difficult for low doses in the presence of ice. In this case the advantage of the PV technique as a real-time method of observation is lost.

Therefore, in order to measure the kinetics of HNO_3 gas in the presence of α-NAT, β-NAT and NAD ice films we have used the two-orifice method first described by Pratte et al. (2006). It has been modified to take into account the interaction of HNO_3 with the internal walls of the SFR. The two-orifice method has also been used to measure the kinetics of H_2O on HNO_3 hydrates in order to compare these results with the results of PV experiments for H_2O.

The two-orifice (TO) method allows the separation of the rate of evaporation $R_{ev}(X)$ and the condensation rate constant $k_c(X)$ of a gas X by choosing two different escape orifices and measuring the corresponding value of concentration $[X]_{SS}$ at steady state of gas X inside the reactor. By alternatively opening the small orifice (S) and both orifices (M) (see Figure 1), two steady state equations hold for a probe gas X which are reported in Eqs. (5) and (6) taking into account the interaction with the reactor walls:

$$R_{ev}(X) + \frac{N_{TOT}}{V} \cdot k_{des,w}(X) \cdot \theta = (k_c(X) + k_{esc}^{S}(X)) \cdot [X]_{SS}^{S} + \frac{k_w(X)}{V} \cdot (1-\theta) \cdot [X]_{SS}^{S} \quad (5)$$

$$R_{ev}(X) + \frac{N_{TOT}}{V} \cdot k_{des,w}(X) \cdot \theta = (k_c(X) + k_{esc}^{M}(X)) \cdot [X]_{SS}^{M} + \frac{k_w(X)}{V} \cdot (1-\theta) \cdot [X]_{SS}^{M} \quad (6)$$

where the superscripts indicate small orifice only (S) or both orifices (M) open, respectively.

The kinetic parameters $R_{ev}(X)$ and $k_c(X)$ are calculated from Eqs. (7) and (8) as follows:

$$k_c(X) = \frac{k_{esc}^{M}(X) \cdot [X]_{SS}^{M} - k_{esc}^{S}(X) \cdot [X]_{SS}^{S}}{[X]_{SS}^{S} - [X]_{SS}^{M}} - k_w(X) \cdot (1-\theta) \quad (7)$$

$$R_{ev}(X) = \frac{(k_{esc}^{M}(X) - k_{esc}^{S}(X)) \cdot [X]_{SS}^{S} \cdot [X]_{SS}^{M}}{[X]_{SS}^{S} - [X]_{SS}^{M}} - \frac{N_{TOT}}{V} \cdot k_{des,w}(X) \cdot \theta \quad (8)$$

This method leads to larger uncertainties for both $R_{ev}(X)$ and $k_c(X)$ compared to the combined PV and steady state method used before. The reason lies in the fact that two similarly large numbers, namely $[X]_{SS}^{S}$ and $[X]_{SS}^{M}$, are subtracted in the denominators of equations Eqs. (7) and (8) leading to a small and therefore uncertain value of $k_c(X)$ and $R_{ev}(X)$. In other words, the noise in the signal from the MS is such that the two data sets for the small orifice and both orifices open are sometimes insufficiently linearly independent of each other within experimental uncertainty.

We also used the combination of real-time PV and steady state experiments using HCl as a probe gas and applied the experimental method described previously in order to measure the kinetics of HCl, $R_{ev}(HCl)$ and $\alpha(HCl)$, in the presence of α-NAT and β-NAT ice films.

Once the kinetics $R_{ev}(X)$ and $k_c(X)$ have been measured using the combination of PV and steady state experiments (H_2O, HCl) or the two-orifice method (HNO_3, H_2O), we may calculate the equilibrium vapor pressure $P_{eq}(X)$ for each gas according to Eq. (9):

$$P_{eq}(X) = \frac{R_{ev}(X)}{k_c(X)} \cdot \frac{RT}{N_A} \quad (9)$$

where R is the molar gas constant in cm^3 Torr K^{-1} mol^{-1}, T the temperature of the thin film in K and N_A Avogadro's constant in molec mol^{-1}.

3 Results

3.1 Crystalline α-NAT Thin Films

The kinetic results for the heterogeneous interaction of H_2O and HNO_3 with α-NAT and NAD thin films obtained in PV and TO experiments are displayed in Figure 2. Full symbols represent PV experiments: full red circles correspond to experiments on α-NAT substrates,

and full green squares to experiments on NAD substrates. Empty symbols represent TO experiments with red circles representing H_2O and black triangles HNO_3 results. Pure ice experiments are displayed as inverse blue triangles for comparison purposes. The calculated relative error for PV experiments is 30% whereas for TO experiments we estimate a relative error of 60%. We refrain at this point from showing raw data (FTIR absorption spectra and MS data as a function of time) because representative samples have been shown by Iannarelli and Rossi (2015) for α- and β-NAT. We will defer the presentation of raw data on the interaction of HCl on α- and β-NAT to Section 3.3 below.

Figure 2a shows the measured accommodation coefficients $\alpha_{\alpha-\mathrm{NAT}}(X)$, ($X = H_2O, HNO_3$), as a function of temperature. $\alpha_{\alpha-\mathrm{NAT}}(H_2O)$ in PV experiments (full red circles) decreases as a function of temperature in the range 167-188.5 K, varying from 0.08 at 167 K to 3.1×10^{-3} at 188.5 K, which is a factor of 30 lower than $\alpha_{ice}(H_2O)$ on pure ice at the same temperature. The scatter in the data is not an artifact and is due to the sample-to-sample variability of the crystalline samples we use and the randomness of the crystalline nucleation process. The variability may be in surface composition, morphology and smoothness as shown in previous studies (McNeill et al., 2007; Iannarelli and Rossi, 2014).

$\alpha_{\alpha-\mathrm{NAT}}(H_2O)$ in TO experiments (empty red circles) yields different results. For temperatures lower than 185 K it is equal to $\alpha_{\alpha-\mathrm{NAT}}(H_2O)$ on α-NAT in PV experiments within experimental error. For temperatures higher than 185 K $\alpha_{\alpha-\mathrm{NAT}}(H_2O)$ increases as a function of temperature in contrast to results of PV experiments (full red circles) varying from 8×10^{-3} at 183 K to 0.08 at 193.5 K, being equal to $\alpha_{ice}(H_2O)$ on pure ice within experimental error at the highest temperature. This result compares favorably with the results of Delval and Rossi (2005) which showed a positive temperature dependence of $\alpha_{\alpha-\mathrm{NAT}}(H_2O)$ in the temperature range 182-207 K. $\alpha_{\mathrm{NAD}}(H_2O)$ in PV experiments (full green squares) is equal within experimental error to $\alpha_{\alpha-\mathrm{NAT}}(H_2O)$.

$\alpha_{\alpha-\mathrm{NAT}}(HNO_3)$ (black empty triangles) increases as a function of temperature in the measured temperature range from a value of approximately 0.005 at 181 K to a value of 0.13 at 188 K. The narrow temperature range follows from the high uncertainties of the two-orifice method at low temperatures and the increasingly rapid conversion of α-NAT to β-NAT at high temperatures. These values are lower by a factor of 2 to 40 compared to the preferred values indicated by the IUPAC Subcommittee on Gas Kinetic Data Evaluation (Crowley et al., 2010).

Figure 2b shows results for the rate of evaporation $R_{ev}(X)$ in molec s^{-1} cm^{-3} as a function of temperature. The same symbols as for panel (a) are used. $R_{ev}(H_2O)$ on α-NAT in PV experiments is lower by a factor of 2 compared to $R_{ev}(H_2O)$ on pure ice at temperatures lower than 175 K. For temperatures higher than 175 K, $R_{ev}(H_2O)$ on α-NAT is lower on average by up to a factor of 50 compared to $R_{ev}(H_2O)$ on pure ice. This result is very different compared to the previously studied case of the binary system HCl amorphous and crystalline hexahydrate using the same apparatus (Iannarelli and Rossi, 2013), where the evaporation of H_2O takes place at a rate characteristic of pure ice despite the presence of adsorbed HCl on the ice and is in agreement with the findings of Delval and Rossi (2005).

$R_{ev}(H_2O)$ on α-NAT measured using the TO method is equal within experimental error to $R_{ev}(H_2O)$ obtained in PV experiments. $R_{ev}(H_2O)$ on NAD is equal to within experimental error to $R_{ev}(H_2O)$ on α-NAT. The full black line shows the rate of evaporation of pure water for the system in use, calculated from literature results of the equilibrium vapor pressure (Marti and Mauersberger, 1993) using $\alpha = 1$, whereas the dashed black line represents extrapolated values of $R_{ev}(H_2O)$ for temperatures lower than 173 K using the expression provided by Mauersberger and coworkers (Marti and Mauersberger, 1993; Mauersberger and Krankowsky, 2003).

Figure 2c shows the results for $P_{eq}(X)$ in Torr calculated according to Eq. (9) for both H_2O and HNO_3 as a function of temperature. The same symbols as in panels (a) and (b) are used. $P_{eq}(H_2O)$ of α-NAT calculated from the kinetic parameters measured in PV experiments is lower by a factor of approximately 3 compared to $P_{eq}(H_2O)$ on pure ice at temperatures higher than 180 K. For temperatures lower than 180 K $P_{eq}(H_2O)$ of α-NAT is close to $P_{eq}(H_2O)$ of pure ice because the present samples are water-rich (Molina, 1994) with a HNO_3 mole fraction of less than 10%.

$P_{eq}(H_2O)$ of α-NAT calculated from the results of TO experiments is lower by up to a factor of 10 compared to $P_{eq}(H_2O)$ of pure ice in the temperature range 180-193.5 K. At temperatures lower than 180 K, $P_{eq}(H_2O)$ of α-NAT from TO experiments is equal within experimental error to $P_{eq}(H_2O)$ of α-NAT in PV experiments. $P_{eq}(HNO_3)$ of α-NAT is lower by a factor of 1000 in the temperature range 181-188 K compared to $P_{eq}(H_2O)$ on pure ice.

The values obtained for the equilibrium vapor pressure have been compared with the HNO_3/H_2O phase diagram constructed by McElroy et al. (1986); Hamill et al. (1988); Molina (1994). Figure 3 shows the results for α-NAT and metastable NAD films, PV and TO

experiments. The solid lines represent the coexistence conditions for two phases and the dashed lines represent vapor pressures of liquids with composition given as % (w/w) of HNO_3. The shaded rectangular area represents typical polar stratospheric conditions. The slope m of the coexistence lines depends on the difference of the enthalpies of sublimation of the two acid hydrate species, namely NAM and NAT, according to Eq. (10) (Wooldridge et al., 1995):

$$m = \frac{\Delta H^1_{subl} - \Delta H^2_{subl}}{(n_1 - n_2)\,R} \qquad (10)$$

where ΔH^1_{subl} and ΔH^2_{subl} are the enthalpies of sublimation of the acid hydrates in kJ/mol, n_1 and n_2 the number of water molecules of the respective hydrate and R is the gas constant in J mol^{-1} K^{-1}. The slope of the ice/NAT coexistence line is calculated from Wooldridge et al. (1995) as $m_{ice/NAT}$ = (50.9 kJ/mol)/R and for NAT/NAM $m_{NAT/NAM}$ = (55.9 kJ/mol)/R.

All α-NAT experiments lie in the existence area of nitric acid trihydrate, as expected. On the other hand, α-NAT under polar stratospheric conditions (shaded rectangular area) is unstable and starts to convert into the stable β-NAT phase (Koehler et al., 1992). The small number of α-NAT samples we reported in the shaded gray area is further confirmation of results reported in the literature because lower temperatures are needed to slow down the conversion of α to β-NAT. NAD samples are expected to lie closer to the monohydrate region, given their composition close to the H_2O:HNO_3 = 2:1 stoichiometry (Iannarelli and Rossi, 2015). Nevertheless, the pure ice phase is still dominant in the present samples and all samples are water-rich (Molina, 1994) with a HNO_3 mole fraction of less than 10% even in NAD films.

3.2 Crystalline β-NAT Thin Films

The results for β-NAT thin films obtained in PV and TO experiments are displayed in Figure 4. Full and empty red squares represent PV and TO experiments, respectively, with red squares representing H_2O and black triangles HNO_3 results. Pure ice experiments are displayed as inverse blue triangles for comparison.

The largest uncertainty in our experiment is that of the flow rate introduced into the reactor, which is assigned a relative error of 25%. The flow rate measurement affects the calibration of the MS and therefore the measurement of all the concentrations in the reactor (Eq. 4). Therefore, we estimate a global relative error of 30% for PV experiments and double this

uncertainty for TO experiments because Equations (7) and (8) imply a difference of two large numbers in many cases, as discussed above. We therefore assign a global 60% relative error to results obtained in TO experiments.

Figure 4a shows the measured $\alpha_{\beta-NAT}(X)$ as a function of temperature: $\alpha_{\beta-NAT}(H_2O)$ resulting from PV experiments (full red squares) is scattered similar to $\alpha_{HH}(HCl)$ on crystalline HCl hexahydrate (Iannarelli and Rossi, 2014) up to a factor of 10 for results at the same temperature. We may interpret this result akin to the HCl hexahydrate case where the scatter may be caused by the variability of the surface composition, the morphology or the smoothness of the ice surface (McNeill et al., 2007). Similar results have recently been presented by Moussa et al. (2013) regarding the nitric acid-induced surface disorder on ice. In any case, all results show that $\alpha_{\beta-NAT}(H_2O)$ is at least a factor of 10 lower than $\alpha_{ice}(H_2O)$ on pure ice in the temperature range 182-200 K.

$\alpha_{\beta-NAT}(H_2O)$ in TO experiments (empty red squares) on the other hand, increases as a function of temperature in the temperature range 182-198 K varying from 0.013 at 182 K to approximately 0.1 at 198 K, being equal at the highest temperature to $\alpha_{ice}(H_2O)$ on pure ice within experimental error. This result is in contrast to Delval and Rossi (2005) who report a negative temperature dependence of $\alpha_{\beta-NAT}(H_2O)$ in the temperature range 182-207 K. A possible reason for the different behavior of PV and TO experiments may be intrinsic in the nature of PV experiments: the ice surface is exposed to a series of pulses of H_2O and the free sites may be saturated before the introduction of each consecutive pulse. We suspect this to be the reason for the discrepancy between PV and TO experiments and we will consider the results of TO experiments as the preferred values of this work despite the larger experimental scatter.

Like $\alpha_{\beta-NAT}(H_2O)$, the values of $\alpha_{\beta-NAT}(HNO_3)$ (black empty triangles) increase as a function of temperature in the measured temperature range from a value of approximately 0.015 at 182 K to a value of 0.08 at 195.5 K. However, the values have a large estimated uncertainty. These values are lower by a factor of 2 to 10 compared to the preferred values indicated by the IUPAC Subcommittee on Gas Kinetic Data Evaluation (Crowley et al., 2010) in the temperature range 190 to 200 K.

Figure 4b shows results for $R_{ev}(X)$ in molec s^{-1} cm^{-3} as a function of temperature. The same symbols as in panel (a) are used. $R_{ev}(H_2O)$ on β-NAT in PV experiments is lower by a factor of 50 compared to $R_{ev}(H_2O)$ on pure ice in the temperature range 182-200 K. As in the case of

α-NAT, this result is very different compared to the case of HCl hydrates studied before using the same apparatus (Iannarelli and Rossi, 2013) where the evaporation of H_2O is not influenced by the presence of adsorbed HCl on the ice and takes place at a rate characteristic of pure ice for all HCl concentrations used.

$R_{ev}(H_2O)$ on β-NAT measured using the TO method is close to $R_{ev}(H_2O)$ obtained in PV experiments, the former being approximately a factor of 2 higher. $R_{ev}(HNO_3)$ on β-NAT increases in the temperature range 182-195.5 K with a steeper slope compared to $R_{ev}(H_2O)$, the former being smaller by approximately a factor of 1000 at 182 K and 50 at 196 K compared to $R_{ev}(H_2O)$ of β-NAT. It varies from 2×10^8 at 182 K to 8.5×10^9 molec s^{-1} cm^{-3} at 195.5 K.

Figure 4c shows the results for $P_{eq}(X)$ in Torr calculated according to Eq. (9) for both H_2O and HNO_3 as a function of temperature. The same symbols as in panels (a) and (b) are used. $P_{eq}(H_2O)$ of β-NAT calculated from the results of TO experiments is lower by up to a factor of 10 in the middle of the covered T-range compared to $P_{eq}(H_2O)$ of pure ice in the temperature range 182-195.5 K. $P_{eq}(H_2O)$ of β-NAT calculated from the kinetic parameters measured in PV agrees with TO experiments within experimental uncertainty. Saturation effects in PV experiments will affect both the accommodation (α) and evaporation (J_{ev}) process to the same extent such that P_{eq} should be invariant to the chosen experimental procedure (PV or TO). However, there is a noticeable scatter in $P_{eq}(H_2O)$ for β-NAT on display in Figure 4c which presumably reflects the range of different compositions of the binary HNO_3/H_2O system. According to Gibb's Phase Rule we have three phases and two components which leads to a single degree of freedom for the system. At constant temperature different HNO_3/H_2O mixing ratios will lead to different values of $P_{eq}(H_2O)$ if we stay on an isotherm. This corresponds to a vertical cut in the binary phase diagram for β-NAT in Figure 5. It shows that we expect $P_{eq}(H_2O)$ values between a factor of ten or so for the experimental points that "fill" the NAT phase diagram more or less homogeneously within the used T range.

In addition, Figure 5 shows that the majority of points are in the rectangular shaded area representing polar stratospheric conditions: β-NAT is the stable phase under these conditions and our results agree well with the literature (McElroy et al., 1986; Hamill et al., 1988; Molina, 1994; Koehler et al., 1992). A more complete manner to display the binary phase diagram is presented in Figure S5 (Supplementary Information). It shows both the HNO_3 and

H_2O partial pressures in one single plot close to selected isotherms marked by straight intersecting dashed lines. It is immediately apparent that both HNO_3 and H_2O partial pressures are comparable to upper tropospheric/lower stratospheric values.

3.3 HCl kinetics on α-NAT and β-NAT Thin Films

As already mentioned, we used a combination of real-time PV and steady state experiments using HCl as probing gas in order to measure the kinetics of HCl interacting with α-NAT and β-NAT ice films. Figure 6 displays raw data from repetitive pulsed dosing of HCl onto an α-NAT/ice substrate as a function of elapsed time. The lower panel displays the MS signals of HCl (red, m/e 36), H_2O (blue, m/e 18) and HNO_3 (black, m/e 46), respectively, and the individual pulses, of which there were twelve, are identifiable by sharp peaks on top of the red columns. Each pulse corresponds to $(4\text{-}5)\times10^{16}$ molecule resulting in a total HCl dose of approximately 3×10^{17} molecules. This is the dose effectively administered to the α-NAT when the fraction of HCl going to the vessel walls and escaping the SFR has been subtracted. This dose approximately corresponds to 1000 molecular monolayers of HCl adsorbed onto the substrate.

The temperature of the cryostat is displayed as the green trace in the lower panel, and with every T-increase the MS steady-state levels of HCl, H_2O and HNO_3 increase concomitantly. (During the pulsed admission of HCl the MS levels of HNO_3 and H_2O are subject to artifacts owing to rapid switching).

Turning to the upper panel of Figure 6 we display a series of FTIR transmission spectra from 700 to 4000 cm^{-1} at specific times during the repetitive pulsing experiment which are indicated in the lower panel by a series of color-coded "sp1" and continuing going from red to purple. The principal peak positions have been collected in Table 3 and will be discussed below in terms of changes in the "pure" α-NAT/ice absorption spectra owing to the presence of increasing adsorbed HCl. The enlarged IR-spectral range in the upper panel of Figure 6 displays the effect of the HCl adsorption particularly well by showing a non-monotonic sequence of IR absorption peaks not present in the "pure" reference spectra from Iannarelli and Rossi (2015). The raw MS data from the lower panel of Figure 6 have been used to calculate the kinetic and thermodynamic data displayed in Figure 8.

Figure 7 displays raw data from repetitive pulsed dosing of HCl onto a β-NAT/ice substrate in analogy to Figure 6. The eleven individual pulses corresponded to $(6\text{-}7)\times10^{16}$ molecule per

519 pulse resulting in a total HCl dose of approximately 4 x 10^{17} molecules which amounts to
520 1300 molecular monolayers or so. Like in Figure 6 the upper panel displays a series of color-
521 coded FTIR absorption spectra in transmission with the principal peak positions collected in
522 Table 3. As for Figure 6 the MS steady-state levels at the different temperatures will be used
523 to derive the kinetic and thermodynamic data of Figure 9 as a function of temperature.

524 In addition, Figure S6 presents an enlarged graph for the non-exponential decay of a HCl
525 pulse interacting with both α- and β-NAT on a 30 s time scale consisting of a fast and a
526 slowly-decaying portion. The evaluation of such pulsed admission MS signals has been
527 presented in the past (Iannarelli and Rossi, 2014, Supplemental Information (SI)) and the
528 present analysis and fitting of the HCl MS signals follows the same scheme.

529 A look at Table 3 should provide an answer as to whether or not there is an identifiable
530 spectral fingerprint of HCl adsorbed on α-or β-NAT in the FTIR absorption spectrum of the
531 combined α- or β-NAT/HCl system displayed in Figure 6 and Figure 7.

532 The first column of Table 3 reveals the spectral fingerprint of HCl for α-NAT/HCl in terms of
533 additional peaks (*in italics*) that are not present in the reference spectrum (pure α-NAT)
534 recorded using the identical instrument and presented in the third column. There seem to be
535 two spectral regions where the presence of HCl may be apparent, namely in the 1618-1644
536 cm^{-1} region corresponding to the broad bending vibration of the proton-ordered waters of
537 hydration (Ritzhaupt and Devlin, 1991; Martin-Llorente et al., 2006), and more importantly,
538 the band at 1328 cm^{-1} that overlaps with the 1339 cm^{-1} vibration, the latter of which is not
539 changing with increasing HCl dose.

540 The series of FTIR absorption spectra displayed in Figure 6 shows the non-monotonous
541 change of intensity at this transition (1328 cm^{-1}): sp1 (red), sp2 (yellow) and sp3 (green)
542 display the growth of a shoulder to the red of the 1375 cm^{-1} peak, sp4 (turquoise), sp5 (blue)
543 and sp6 (purple) show the separate peak in its decline (1328 cm^{-1}) owing to evaporation of
544 HCl together with NAT.

545 For β-NAT the analogous situation is displayed in the second and fourth column of Table 3
546 and Figure 7. Here the presence of HCl is more discrete within the FTIR absorption spectrum
547 of β-NAT as Table 3 suggests the well-separated peak to the blue of the 3227 cm^{-1} ice peak at
548 3360 cm^{-1} to be a HCl tracer as it looks very similar to the HCl/H_2O system (Iannarelli and
549 Rossi, 2014; Chiesa and Rossi, 2013). The peaks identified to appear in the FTIR spectrum

upon HCl adsorption may be found in the fifth column of Table 3 which displays the principal IR peaks in the reference HCl/H_2O system, except the 1200 cm^{-1} vibration found in column 1 and 2 whose origin remains unclear.

In order to restrain the number of independent measurements on this ternary system to a practical level we had to make some assumptions and/or simplifications in order to measure the unknown parameters of Eq. (2) for each gas used. Specifically, we made the following reasonable assumptions, both for α-NAT and β-NAT substrates which have been experimentally verified in laboratory experiments:

- $R_{ev}(H_2O)$ on NAT remains unchanged in the presence of HCl
- $\alpha_{NAT}(H_2O)$ remains unchanged in the presence of HCl
- $\alpha_{NAT}(HNO_3)$ remains unchanged in the presence of HCl

Under these assumptions, no additional measurements of the heterogeneous kinetics of H_2O in the presence of HCl have been performed. We have measured the steady-state flow $F_{SS}(HNO_3)$ before each HCl pulse series and used previously measured $\alpha_{\alpha-NAT}(HNO_3)$ and $\alpha_{\beta-NAT}(HNO_3)$ from TO experiments on α-NAT and β-NAT phases in order to calculate $R_{ev}(HNO_3)$ and $P_{eq}(HNO_3)$ according to Eqs. (8) and (9) in HCl-PV experiments as well. As a net result we measure or calculate the following kinetic parameters for α-NAT and β-NAT substrates: $R_{ev}(HCl)$, $\alpha_{NAT}(HCl)$ and $R_{ev}(HNO_3)$ in the presence of HCl.

Figure 8 displays the results of HCl-PV experiments on α-NAT substrates. Full red diamonds represent the results for HCl whereas full black circles represent HNO_3 results using $\alpha_{\alpha-NAT}(HNO_3)$ from TO experiments and $F_{SS}(HNO_3)$ from HCl-PV experiments. Empty black triangles represent results for HNO_3 in TO experiments reported from Figure 2 for comparison.

Figure 8a displays the measured $\alpha_{\alpha-NAT}(X)$ as a function of temperature. $\alpha_{\alpha-NAT}(HCl)$ (full red diamonds) slightly decreases as a function of temperature in the range 177.5-199.5 K, being equal to $\alpha_{ice}(H_2O)$ on pure ice at low temperatures and lower by a factor of 4 at T = 199.5 K. The decrease seems to be significant. Values of $\alpha_{\alpha-NAT}(HNO_3)$ measured in TO experiments in the absence of HCl are reported as empty black triangles in agreement with the third above-listed assumptions. We used these values in order to calculate $R_{ev}(HNO_3)$ and $P_{eq}(HNO_3)$ in the presence of HCl.

Figure 8b shows results for $R_{ev}(X)$ in molec s^{-1} cm^{-3} as a function of temperature. The same symbols as in panel (a) are used. $R_{ev}(HCl)$ on α-NAT slightly increases as a function of temperature, but is lower by a factor of 1000 in the measured temperature range 177.5-199.5 K compared to $R_{ev}(H_2O)$ on pure ice. $R_{ev}(HNO_3)$ increases as a function of temperature, varying from 1×10^8 at 181 K to 9×10^9 molec s^{-1} cm^{-3} at 189 K. The presence of HCl does not have any effect on the rate of evaporation of HNO_3 from α-NAT films: we observe no increase of $F_{ss}(HNO_3)$ following HCl pulses and $R_{ev}(HNO_3)$ in the presence of adsorbed HCl molecules (full black circles) is identical within experimental error to $R_{ev}(HNO_3)$ of α-NAT films free of adsorbed HCl (empty black triangles). However, this result is contingent upon the assumptions listed before, namely $\alpha_{\alpha-NAT}(HNO_3)$ being independent of the presence or absence of HCl.

Figure 8c shows the results for $P_{eq}(X)$ in Torr calculated according to Eq. (9) for both HCl and HNO_3 as a function of temperature. The same symbols as in panel (a) and (b) are used. $P_{eq}(HCl)$ for HCl-doped α-NAT is lower by a factor of approximately 100 compared to $P_{eq}(H_2O)$ on pure ice in the measured temperature range. A comparison with the results of $P_{eq}(HCl)$ of crystalline HCl hexahydrate and amorphous HCl/H_2O mixtures calculated using the same experimental methodology (Iannarelli and Rossi, 2014) shows that $P_{eq}(HCl)$ of HCl-doped α-NAT is lower by a factor of approximately 10 compared to $P_{eq}(HCl)$ of crystalline hexahydrate in the overlapping temperature range (177.5-193.5 K).

$P_{eq}(HCl)$ of amorphous HCl/H_2O mixtures is higher by a factor of 20 compared to $P_{eq}(HCl)$ of HCl-doped α-NAT at low temperatures (177.5 K) with the difference being constant or slightly decreasing at high temperatures (199.5 K) where $P_{eq}(HCl)$ of the amorphous mixture is only a factor of 4 higher than $P_{eq}(HCl)$ of α-NAT.

$P_{eq}(HNO_3)$ on HCl-doped α-NAT films is equal within experimental error to $P_{eq}(HNO_3)$ of α-NAT films free of adsorbed HCl. It is lower by a factor of 1000 compared to $P_{eq}(H_2O)$ on pure ice in the measured temperature range 177.5-199.5 K.

Figure 9a (symbols have the same meaning as in Figure 8) shows the measured values of $\alpha_{\beta-NAT}(X)$ as a function of temperature. $\alpha_{\beta-NAT}(HCl)$ slightly decreases as a function of temperature in the range 177-201 K, varying from 0.025 at 177 K to 0.016 at 201 K which may or may not be significant. As for the case of α-NAT, we assume that $\alpha_{\beta-NAT}(HNO_3)$

(empty black triangles) equals the measured values of $\alpha_{\beta-NAT}(HNO_3)$ on HCl-free β-NAT in two-orifice experiments whose results are displayed in Figure 4a.

Figure 9b shows results for the $R_{ev}(X)$ in molec s^{-1} cm^{-3} as a function of temperature. The same symbols as in Panel (a) are used. $R_{ev}(HCl)$ on β-NAT is equal at higher temperature within experimental uncertainty to $R_{ev}(HCl)$ on α-NAT and is lower by a factor of 1000 in the temperature range 177- 201 K compared to $R_{ev}(H_2O)$ on pure ice. $R_{ev}(HNO_3)$ on HCl-doped β-NAT films, being equal within experimental error to $R_{ev}(HNO_3)$ of undoped β-NAT films, indicates that adsorbed HCl molecules seem to have no effect on the rate of evaporation of HNO_3 from β-NAT films in the presence of HCl as well, at least in the given T range.

Figure 9c shows the results for $P_{eq}(X)$ in Torr calculated according to Eq. (9) for both HCl and HNO_3 as a function of temperature. The same symbols as in panel (a) and (b) are used. $P_{eq}(HCl)$ of HCl-doped β-NAT is lower by a factor of approximately 100 compared to $P_{eq}(H_2O)$ on pure ice. $P_{eq}(HCl)$ of HCl-doped β-NAT is identical within experimental uncertainty to $P_{eq}(HCl)$ of HCl-doped α-NAT in the measured temperature range 177-201 K and the same observations are valid when comparing $P_{eq}(HCl)$ of crystalline HCl hexahydrate with amorphous HCl/H_2O mixtures (Iannarelli and Rossi, 2014).

4 Discussion

In this work we have been able to grow HNO_3 hydrates at temperatures relevant to the stratosphere with tight control on the deposition conditions whose details have been published by Iannarelli and Rossi (2015) as far as the mass balance is concerned. Spontaneous crystallization of α-NAT film on pure ice has been observed upon HNO_3 deposition. Under the present conditions β-NAT was never observed to crystallize directly upon HNO_3 deposition but was always obtained as the stable form after conversion of α-NAT films. Temperatures higher than 185 K are necessary for the conversion to occur on the time scale of the experiments we have performed.

$\alpha_{\alpha-NAT}(H_2O)$ shows two distinct temperature dependent regimes. At temperatures lower than 180-185 K it decreases as a function of temperature reaching a minimum of approximately 0.003 at 185 K as displayed in Figure 2a. For temperatures higher than 185 K, $\alpha_{\alpha-NAT}(H_2O)$ increases as a function of temperature, being equal to $\alpha_{ice}(H_2O)$ on pure ice and $\alpha_{\beta-NAT}(H_2O)$ at 193.5 K. An Arrhenius representation of the evaporative flux $J_{ev}(H_2O)$ (see Table 1) on α-NAT shows two distinct regimes of temperature dependence, as well. Figure 10 reports the

results for PV and TO experiments as full and empty red circles, respectively. We keep the two data sets separated for clarity, but the results of PV and TO experiments are indistinguishable within experimental uncertainty in the measured temperature range.

Eqs. (11) and (12) present the two-parameter representations of the Arrhenius lines for $J_{ev}(H_2O)$ displayed in Figure 10. Equations (11) and (12) represent the solid and dashed red lines, respectively, with R = 8.314 J K^{-1} mol^{-1} used throughout:

$$181\ \mathrm{K} \leq \mathrm{T} \leq 193.5\ \mathrm{K}:\ \log J_{ev}(H_2O)[\mathrm{molec}\cdot\mathrm{cm}^{-2}\cdot\mathrm{s}^{-1}] = (35.9 \pm 2.8) - \frac{(75.3 \pm 9.9)\times 10^3}{2.303\ \mathrm{RT}} \quad (11)$$

$$167\ \mathrm{K} \leq \mathrm{T} \leq 181\ \mathrm{K}:\ \log J_{ev}(H_2O)[\mathrm{molec}\cdot\mathrm{cm}^{-2}\cdot\mathrm{s}^{-1}] = (15.1 \pm 1.2) - \frac{(3.5 \pm 4.2)\times 10^3}{2.303\ \mathrm{RT}} \quad (12)$$

Table 4 reports a synopsis of the kinetic (J_{ev}) as well as the thermodynamic (P_{eq}) parameters calculated for all experiments of the present work.

The considerable scatter in the kinetic data, reflected in the significant uncertainties of Eqs. (11) and (12), may be explained by the variability of the surface composition of the film as well as the surface roughness and surface disorder of the ice substrates, in analogy to the HCl case (Iannarelli and Rossi, 2014). For HCl the scatter in the kinetic data was thought to be due to the stochastic nature of crystal growth of hexahydrate films compared to amorphous mixtures of HCl/H_2O of similar composition and does not represent a lack of reproducibility.

Moussa et al. (2013) have observed variations of up to a factor of 10 of the HNO_3 vapor pressure of "smooth" ice samples exposed to HNO_3 as a result of induced surface disorder. The exposure of the present samples to repeated high H_2O supersaturation during PV experiments may lead to surface increased disorder due to liquefaction and/or reconstruction. In the high temperature regime we calculate an activation energy for H_2O evaporation $E_{ev}(H_2O)$ = (75.3 ± 9.9) kJ mol^{-1}, and in the low temperature regimes almost no temperature dependence is observed with an activation energy for H_2O evaporation of $E_{ev}(H_2O)$ = (3.5 ± 4.2) kJ mol^{-1}.

The discontinuity in the Arrhenius representation of kinetic parameters has already been observed in pure ice as reported by Chaix et al. (1998); Delval et al. (2003); Delval and Rossi (2004); Pratte et al. (2006). The temperatures at which the discontinuity occurs are higher in previous work: Delval et al. (2003) reported a discontinuity at approximately 208 K in their work on H_2O evaporation from HCl and HBr doped ice substrates. In a quartz crystal microbalance study of H_2O evaporation from pure ice the change in slope is reported at 193 ±

2 K (Delval and Rossi, 2004) comparable with the temperature of 188 ± 2 K reported by Pratte et al. (2006) in their work on the kinetics of H_2O evaporation and condensation on different types of ice.

No clear explanation for this break has yet been advanced. The discontinuity may be an indication of the formation of a new disordered structure similar to the quasi-liquid layer induced by HCl as proposed by McNeill et al. (2006). The observation of the break in pure ice samples as well, however, strongly suggests that the onset of a quasi-liquid layer may be independent of the presence of HCl and that the history and evolution of the sample play a role in the arrangement of the structure, similarly to the case of the presence of cubic ice at high temperature in common hexagonal ice that finally turned out to be a perturbed hexagonal ice structure (Kuhs et al., 2012).

In the case of β-NAT we have good agreement between PV (dotted line) and TO (solid line) experiments of $P_{eq}(H_2O)$ as shown in the van 't Hoff representation displayed in Figure 11.

As already mentioned, the ice surface is exposed to a series of pulses of H_2O during PV experiments. The free sites may be saturated before the introduction of each consecutive pulse resulting in the discrepancy between PV and TO experiments. We therefore believe that the results from PV experiments are more precise but less accurate owing to partial surface saturation whereas the TO experiments are less precise but more accurate. We chose the latter as the preferred values of this work despite the larger scatter in the data compared to the PV experiments.

Eqs. (13) and (14) reports the best linear fit for TO and PV experiments on β-NAT displayed in Figure 11, respectively:

$$\log P_{eq}(H_2O)[\text{Torr}] = (16.7 \pm 4.9) - \frac{(76.7 \pm 17.7)\times 10^3}{2.303\ RT} \qquad \text{TO – Preferred} \qquad (13)$$

$$\log P_{eq}(H_2O)[\text{Torr}] = (16.7 \pm 3.0) - \frac{(75.5 \pm 11.1)\times 10^3}{2.303\ RT} \qquad \text{PV} \qquad (14)$$

The enthalpies of evaporation of H_2O on β-NAT films calculated for the two measurement techniques are $\Delta H^0_{ev,TO}(H_2O)$ = (76.7 ± 17.7) kJ mol^{-1} for TO and $\Delta H^0_{ev,PV}(H_2O)$ = (75.5 ± 11.1) kJ mol^{-1} for PV experiments, respectively. The results show good agreement between the two experimental techniques despite the experimental scatter. The average value of $\Delta H^0_{ev}(H_2O)$ = (76.1 ± 14.4) kJ mol^{-1} is slightly higher, as expected, but not significantly different compared to α-NAT films. Figure S2 of Supplement C displays a van't Hoff plot for

α-NAT with $\Delta H^0_{ev}(H_2O)$ = (70.3 ± 14.1) and (56.5 ± 5.1) kJ mol^{-1} for TO and PV experiments, respectively. Both values are identical within experimental uncertainty whose average yields $\Delta H^0_{ev}(H_2O)$ = (63.4 ± 9.6) kJ mol^{-1} and which leads to a standard enthalpy of formation slightly larger than that for β-NAT, as expected.

However, we do not have good agreement between TO and PV experiments for the kinetic parameters of β-NAT: a discrepancy is observed in the results of the two measurement techniques regarding $R_{ev}(H_2O)$ and $\alpha(H_2O)$ for β-NAT. Figure 4 already shows a discrepancy in $\alpha(H_2O)$ (full and empty red squares in panel a) with the results of TO experiments being larger by a factor of approximately 5 at 185 K increasing to a factor of 100 at 200 K compared to PV experimental results across the whole temperature range. The same qualitative trend, albeit to a smaller extent, is observed for $R_{ev}(H_2O)$ (Figure 4b) and the Arrhenius representation of $J_{ev}(H_2O)$ on β-NAT clearly shows the discrepancy between the different measurement techniques.

The two-parameter representations of the Arrhenius lines displayed in Figure 12 for β-NAT are reported in Eqs. (15) and (16) for TO (solid line) and PV (dotted line) experiments, respectively:

$$\log J_{ev}(H_2O)[\text{molec} \cdot \text{cm}^{-2} \cdot \text{s}^{-1}] = (36.0 \pm 1.3) - \frac{(77.0 \pm 4.9)\times 10^3}{2.303\ \text{RT}} \quad \text{TO – Preferred} \qquad (15)$$

$$\log J_{ev}(H_2O)[\text{molec} \cdot \text{cm}^{-2} \cdot \text{s}^{-1}] = (28.7 \pm 0.7) - \frac{(52.1 \pm 2.4)\times 10^3}{2.303\ \text{RT}} \quad \text{PV} \qquad (16)$$

Contrary to the case of α-NAT, no discontinuity in $J_{ev}(H_2O)$ has been observed in the Arrhenius plot of β-NAT displayed in Figure 12. We attribute the discrepancy between PV and TO experiments to the fact that the former may be subject to partial saturation of uptake and evaporation in the aftermath of transient supersaturation (PV). A look at the results of $\alpha_{\alpha-NAT}(H_2O)$ in Figure 2a reveals that the results of the TO measurement technique agrees well with the PV technique in the overlapping temperature range. However, this plot displays a "hole" of a factor of 20 centered in the neighborhood of T = 180 ± 3 K with respect to the values at the fringes of the temperature interval. There are indications that PV experiments on α-NAT substrates may yield lower values of $\alpha_{\alpha-NAT}(H_2O)$ at high temperatures in excess of approximately 182 K (Figure 2a), similarly to the results for $\alpha_{\beta-NAT}(H_2O)$ for a β-NAT film (Figure 4a). This might be an indication that PV experiments are very sensitive to the interfacial nature of the sample. In other words, transient supersaturation (PV) and "passive"

steady-state (TO) experiments may address different properties of the gas-condensed surface interface. This is the first time such a large discrepancy between two kinetic measurements techniques has been observed. As expected, thermodynamic results are not affected for reasons of microscopic reversibility because both forward ($\alpha(H_2O)$) and reverse reactions ($J_{ev}(H_2O)$) are affected to the same extent which cancels out for the calculation of the values of thermodynamic parameters.

Figure S3 of Supplement C shows the results of PV experiments using H_2O as a probe gas on α-NAT and β-NAT substrates. Red and black circles represent the decay of series of two pulses on α- and β-NAT, respectively, with the first and second pulse labeled accordingly. In the case of α-NAT films (red circles), the decay of the second pulses is equal to within 20-30% of the decay of the initial pulses, and only in a few cases at temperatures higher than 180 K is the decay of the second pulse significantly slower than the initial pulse. In the case of β-NAT films, the decay of second pulses is consistently slower than the decay of first pulses in most cases. This indicates that the surface of β-NAT films exposed to a transient supersaturation of H_2O vapor is more prone to saturation compared to α-NAT.

As mentioned before, we consider the results of TO experiments preferred for β-NAT this work despite its larger uncertainty. The enthalpies of evaporation $\Delta H^0_{ev,TO}(H_2O)$ = (76.7 ± 17.7) kJ mol^{-1} and the activation energy for evaporation $E_{ev}(H_2O)$ = (77.0 ± 4.9) kJ mol^{-1} are equal to within experimental uncertainties. We calculate an activation energy of accommodation for H_2O on β-NAT of $E_{acc}(H_2O) = E_{ev}(H_2O) - \Delta H^0_{ev,TO}(H_2O) = 0$. Therefore, no activation energy is required for the accommodation process of H_2O on β-NAT which is an expected experimental outcome. In contrast, the activation energy for H_2O accommodation on α-NAT is computed as $E_{acc}(H_2O) = E_{ev}(H_2O) - \Delta H^0_{ev,average}(H_2O)$ = 75.3 – 63.4 = 11.9 kJ/mol when using a value averaged over the PV and TO experiment of 63.4 kJ/mol for $\Delta H^0_{ev,average}(H_2O)$. This small, but possibly significant positive activation energy is consistent with the positive temperature dependence of $\alpha_{\alpha-NAT}(H_2O)$ displayed in Figure 2a for the TO experiment at T > 182 K, that is in the high T-range.

$R_{ev}(H_2O)$ on both α-NAT and β-NAT is smaller compared to $R_{ev}(H_2O)$ on pure ice. This is in agreement with the results of Tolbert and Middlebrook (1990), Middlebrook et al. (1996), Warshawsky et al. (1999) and Delval and Rossi (2005) who showed that ice coated with a number of molecular layers of NAT evaporates H_2O at a slower rate than pure ice. On the

other hand, our results are in contrast with the findings of Biermann et al. (1998) who report that no significant decrease of the H_2O evaporation rate was observed in HNO_3-doped ice films. The discrepancy may possibly be caused by the high total pressure of 0.85 mbar in their reactor compared to all other competitive studies cited above that use high-vacuum chambers with total pressures lower by typically a factor of 500 or more.

It is very likely that the experiments performed by Biermann et al. (1998) were not sensitive to changes in evaporation rates despite the fact that both the HNO_3 and H_2O concentrations used as well as the thickness of the accumulated NAT layers in their no. 5 experiment were of the same magnitude as in the competing studies. A hint to that effect is the unexpected time dependence of the ice evaporation rate in Biermann et al. (1998) that shows an induction time of 30 minutes as opposed to the expected linear decrease from the beginning of evaporation (see below). We are unable to attribute the source of the measured H_2O vapor in the presence of two H_2O-containing solid phases in our chemical system, namely pure H_2O ice and NAT. We restate that the partial pressures at constant temperature are controlled by the (relative) composition of the system in agreement with the single degree of freedom resulting from Gibb's Phase Rule and the data displayed in the binary HNO_3/H_2O phase diagrams displayed in Figure 3, Figure 5 and Figure S5.

Delval and Rossi (2005) report that the initial evaporation of H_2O in their experiments was always that of pure ice and that $R_{ev}(H_2O)$ gradually decreases with the evaporation of excess H_2O and the increase in the average HNO_3 mole fraction. They refer to this difference as "high and low evaporation rate" regime of H_2O. Our observation is somewhat different compared to Delval and Rossi (2005): $R_{ev}(H_2O)$ on α-NAT and β-NAT is smaller compared to $R_{ev}(H_2O)$ on pure ice over the whole temperature range and for all samples. The reason lies in the fact that the average mole fraction of HNO_3 of the present samples is higher by at least a factor of 10 compared to the one used by Delval and Rossi (2005). Therefore all our samples are in the "low evaporation rate" regime of H_2O and our results compare well with the results of Delval and Rossi (2005) once they evaporate excess H_2O and reach the "low evaporation rate" regime.

Figure 13 displays both the Arrhenius plots of $J_{ev}(HNO_3)$ (A) and the van 't Hoff plots of $P_{eq}(HNO_3)$ (B) for the interaction of HNO_3 with α- and β-NAT films. We would like to briefly remind the reader that only TO experiments were possible for HNO_3 experiments because no sharp pulses could be generated with pure HNO_3, presumably owing to the

tendency of nitric acid to stick to the inner surfaces, mainly on stainless (austenitic) steel. This has been verified by measuring the Langmuir adsorption on that same surface (Figure S1, Table 2). The following equations define the corresponding straight lines based on the present measurements. For α-NAT (Eqs. (17) and (18)) and β-NAT (Eqs. (19) and (20)) films we find the following results:

α-NAT: $$\log J_{ev}(HNO_3)[\text{molec} \cdot \text{cm}^{-2} \cdot \text{s}^{-1}] = (62.3 \pm 7.8) - \frac{(178.0 \pm 27.4)\times 10^3}{2.303\ \text{RT}} \quad (17)$$

$$\log P_{eq}(HNO_3)[\text{Torr}] = (29.3 \pm 12.0) - \frac{(128.6 \pm 42.4)\times 10^3}{2.303\ \text{RT}} \quad (18)$$

β-NAT: $$\log J_{ev}(HNO_3)[\text{molec} \cdot \text{cm}^{-2} \cdot \text{s}^{-1}] = (40.6 \pm 2.4) - \frac{(102.0 \pm 8.6)\times 10^3}{2.303\ \text{RT}} \quad (19)$$

$$\log P_{eq}(HNO_3)[\text{Torr}] = (19.8 \pm 3.3) - \frac{(96.5 \pm 12.0)\times 10^3}{2.303\ \text{RT}} \quad (20)$$

We calculate an activation energy for HNO_3 evaporation on α-NAT and β-NAT of $E_{ev}(HNO_3)$ = (178.0 ± 27.4) kJ mol^{-1} and $E_{ev}(HNO_3)$ = (102.0 ± 8.6) kJ mol^{-1}, respectively. These values are higher compared to $E_{ev}(HCl)$ = (87.0 ± 17) kJ mol^{-1}, the activation energy for HCl evaporation on hexahydrate. This result is within expectation given the higher hydrogen bond energy of HNO_3 compared to HCl with H_2O.

Similar to the case of H_2O, no activation energy for accommodation of HNO_3 on β-NAT is required since the evaporation activation energy $E_{ev}(HNO_3)$ = (102.0 ± 8.6) kJ mol^{-1} and the enthalpy of evaporation $\Delta H^0_{ev}(HNO_3)$ = (96.5 ± 12.0) kJ mol^{-1} are equal within experimental uncertainty. In contrast, a substantial activation energy of HNO_3 mass accommodation of 49.4 kJ/mol is calculated from $E_{acc}(HNO_3) = E_{ev}(HNO_3) - \Delta H^0_{ev,\,TO}(HNO_3)$ = 178.0 – 128.6 = 49.9 kJ/mol which may have to do with the fact that α-NAT is metastable owing to its unstable H_2O crystal structure (Weiss et al., 2016).

The thermodynamic parameters obtained above, namely $\Delta H^0_{ev}(H_2O)$ and $\Delta H^0_{ev}(HNO_3)$ for both α- and β-NAT may now be used to estimate the relative stability of α- vs. β-NAT as follows. The evaporation/condensation equilibrium for both forms of NAT may be represented in equation (21) where $\Sigma\Delta H_{ev}{}^0 = 3\,\Delta H^0_{ev}(H_2O) + \Delta H^0_{ev}(HNO_3)$ in agreement with the relevant stoichiometry:

$$HNO_3 \bullet 3H_2O(s) \leftrightarrows 3H_2O(g) + HNO_3(g) \qquad (\Sigma\Delta H_{ev}{}^0) \quad (21)$$

For α- and β-NAT we obtain $\Sigma\Delta H_{ev}^{0,\alpha}$ and $\Sigma\Delta H_{ev}^{0,\beta}$ equal to 318.8 and 324.8 kJ/mol, respectively, when we use the average of the TO and PV experiment for H_2O and the TO value listed above for HNO_3 evaporation. Specifically, we have used (63.4 ± 9.6) and (128.6 ± 42.2) for H_2O- and (76.1 ± 14.4) and (96.5 ± 12.0) for HNO_3-evaporation for α- and β-NAT, respectively, as displayed above. Finally, we arrive at the difference $\Sigma\Delta H_{ev}^{0,\alpha}$ - $\Sigma\Delta H_{ev}^{0,\beta}$ = -6.0 ± 20.0 kJ/mol which shows that β-NAT is marginally more stable than α-NAT. This is true despite the fact that the standard heat of evaporation for HNO_3 in α-NAT ($\Delta H_{ev}^{0}(HNO_3)$) is significantly larger than for β-NAT by 32.1 kJ/mol which may be expressed by the fact that the calculated "affinity" of HNO_3 towards ice in the α-NAT is larger than for β-NAT as claimed by Weiss et al. (2016). However, this fact only addresses the behavior of HNO_3 without taking into consideration the partial stability of the H_2O network in the total crystal structure. In view of the large uncertainty, mainly brought about by the TO experiment, we regard this result as an estimate to the true standard enthalpy difference between α- and β-NAT.

The results of HCl kinetic measurements displayed in Figure 8 and Figure 9 show that $R_{ev}(HCl)$ is always higher than $R_{ev}(HNO_3)$, with the latter being equal regardless of the presence of absorbed HCl molecules in the condensed phase. Hynes et al. (2002) observed that HCl uptake on HNO_3 dosed ice was always nearly reversible in their experiments, in contrast to HCl uptake on clean ice. Although the same HNO_3 dosed ice surface has been dosed repeatedly at different HCl concentrations by Hynes et al. (2002), the degree of reversibility was found to be unaffected by previous experiments. In contrast, we never observed such reversibility. In our experiments, HCl always remained on the surface, evaporating at a rate only slightly faster than HNO_3 both for α-NAT and β-NAT and similarly to $R_{ev}(HCl)$ of crystalline hexahydrate (Iannarelli and Rossi, 2014). However, a possible influence of the temperature cannot be excluded at this time, as the experiments performed by Hynes et al. (2002) have been performed at distinctly higher temperatures, namely in the range 210-235 K, compared to the experiments discussed here.

Similar behavior has been observed by Kuhs et al. (2012) with respect to the presence of cubic ice or "ice I_c" in common hexagonal ice I_h. I_h is expected to be the prevalent ice phase at temperatures relevant to atmospheric processing on thermodynamic grounds. Apparent formation of I_c has been observed over a wide temperature range and evidence pointed towards the fact that the resulting phase is not pure cubic ice but instead composed of

disordered cubic and hexagonal stacking sequences. Kuhs et al. (2012) studied the extent and relevance of the stacking disorder using both neutron as well as X-ray diffraction as indicators of the "cubicity" of vapor deposited ice at temperatures from 175 to 240 K and could simply not find proof for the formation of cubic ice I_c under atmospheric conditions.

Kuhs et al. (2012) discovered that even at temperatures as high as 210 K, the fraction of cubic sequences in vapor deposited ice is still approximately 40%. The rate of decrease in cubicity depends on the temperature, being very slow at temperatures lower than 180 K and increasingly rapid at temperatures higher than 185 K. Furthermore, even at high temperatures the complete transformation into pure ice I_h was never observed, with a few percent of cubic stacking sequences still remaining in the ice, even after several hours at 210 K and disappeared only upon heating to 240 K. In addition, the combination of neutron and X-ray diffraction experiments of Kuhs et al. (2012) cannot distinguish the difference between the bulk and the interface whereas our measurement techniques, in particular PV experiments, are very sensitive to the nature and properties of the sample interface.

In light of these results we speculate that the presence of two hydrates of HNO_3, namely α-NAT and β-NAT, may depend on the cubicity or stack-disorder of the ice upon which the NAT grows. HNO_3 adsorbed on cubic ice I_c tends to form α-NAT crystalline structures which upon heating converts to β-NAT while the ice loses part of its cubicity. The temperature at which the conversion from α-NAT to β-NAT is accelerated, T = 185 K, is the same temperature Kuhs et al. (2012) report as the temperature at which the rate of decrease in cubicity increases. Our hypothesis is that the formation of α-NAT or β-NAT may highly depend on the environment in which the NAT phase grows and on the presence of high or low fractions of "I_c".

Figure 14 displays both the Arrhenius plots of J_{ev}(HCl) (A) and the van 't Hoff plots of P_{eq}(HCl) (B) for the interaction of HCl with α-NAT and β-NAT films. As for the case of HNO_3, only TO experiments were performed with HCl as a probe gas. Full red circles and black triangles represent the interaction of HCl with α- and β-NAT films, respectively.

The following equations define the corresponding straight lines resulting from the present measurements. For α-NAT (Eqs. (22) and (23)) and β-NAT films (Eqs. (24) and (25)) we find the following results:

α-NAT: $$\log J_{ev}(\mathrm{HCl})[\mathrm{molec}\cdot\mathrm{cm}^{-2}\cdot\mathrm{s}^{-1}] = (34.8 \pm 5.3) - \frac{(78.3 \pm 19.2)\times 10^3}{2.303\ \mathrm{RT}} \qquad (22)$$

$$\log P_{eq}(HCl)[\text{Torr}] = (15.7 \pm 3.2) - \frac{(78.4 \pm 11.4)\times 10^3}{2.303\ RT} \quad (23)$$

β-NAT: $$\log J_{ev}(HCl)[\text{molec} \cdot \text{cm}^{-2} \cdot \text{s}^{-1}] = (28.6 \pm 1.3) - \frac{(56.7 \pm 4.6)\times 10^3}{2.303\ RT} \quad (24)$$

$$\log P_{eq}(HCl)[\text{Torr}] = (13.3 \pm 1.6) - \frac{(69.6 \pm 5.8)\times 10^3}{2.303\ RT} \quad (25)$$

Despite the considerable scatter of the data displayed in Figure 14 it may be pointed out that the enthalpy of HCl evaporation is identical for α- and β-NAT within the stated experimental uncertainty: We compare $\Delta H^0_{ev}(HCl)$ of 78.4 ± 11.4 and 69.6 ± 5.8 kJ/mol for α- and β-NAT (equations (23) and (25)). On the other hand, we have equality, perhaps fortuitously, between $E_{ev}(HCl)$ and $\Delta H^0_{ev}(HCl)$ for α-NAT following equations (22) and (23) which leads to the conclusion that HCl accommodation on α-NAT is not an activated process with essentially zero activation energy similar to the situation for HNO_3 interacting with β-NAT. On the other hand, this type of argument would lead to a negative activation energy for HCl accommodation on β-NAT because the enthalpy of evaporation of HCl from β-NAT is smaller than $E_{ev}(HCl)$ from β-NAT.

However, the kinetic data of $J_{ev}(HCl)$ for β-NAT may be affected by saturation of HCl uptake because experiments have been performed using the PV admission. This situation may be similar to the kinetic results of $J_{ev}(H_2O)$ for β-NAT displayed in Figure 12 that shows a significantly smaller value for $E_{ev}(H_2O)$ in PV vs. TO experiments (52.1 vs. 75.5 kJ/mol, see also Table 4) whereas the saturation effect seems not to affect the kinetic data for α-NAT. The anomalously large experimental uncertainty for HNO_3 TO experiments on α-NAT displayed in Table 4 certainly has to do with the restricted temperature interval over which we were able to monitor α-NAT before it converted to β-NAT. This may be seen in the synoptic overview of the van't Hoff plots for HNO_3 interacting with NAT displayed in Figure S4 of Supplement D. This restricted T range is also visible in Figure 13A for $J_{ev}(HNO_3)$ from α-NAT..

5 Atmospheric implications and conclusion

In this study we have confirmed that exposure of ice films to HNO_3 vapor pressures at temperatures found in the stratosphere leads to formation of NAT hydrates.

Of the two known forms of NAT, namely α-NAT and β-NAT, the latter is the thermodynamically stable one whereas metastable α-NAT is likely to be of lesser importance in the heterogeneous processes at UT/LS atmospherically relevant conditions.

$R_{ev}(H_2O)$ on α-NAT and β-NAT films are very different compared to the case of HCl/ice where the evaporation of H_2O is not influenced by the presence of adsorbed HCl on the ice and takes place at a rate characteristic of pure ice. This has important implications on the lifetime of atmospheric ice particles. Ice particles with adsorbed HNO_3 forming NAT have longer lifetimes compared to ice particles with adsorbed HCl, being amorphous or crystalline $HCl \bullet 6H_2O$. In light of our results we raise the question if HCl-containing ice particles are of significant atmospheric relevance as substrates for heterogeneous reactions due to their reduced lifetimes and concurrent reduced opportunities to enable heterogeneous atmospheric reactions such as Reaction (1).

$J_{ev}(H_2O)$ on α-NAT presents a discontinuity at 185 K akin to that observed in pure ice by Delval and Rossi (2004); Pratte et al. (2006). The resulting Arrhenius representation at high temperatures larger than 181 ± 2 K is:

$$\log J_{ev}(H_2O)[\text{molec} \cdot \text{cm}^{-2} \cdot \text{s}^{-1}] = (35.9 \pm 2.8) - \frac{(75.3 \pm 9.9) \times 10^3}{2.303\ \text{RT}} \quad (11)$$

$J_{ev}(H_2O)$ on β-NAT shows two values depending on the measurement techniques as a result of the propensity of the PV experiment to saturate the gas-condensate interface. TO experiments are less precise but more accurate owing to the fact that they are less prone to saturation compared to PV experiments. Therefore, we report results of TO experiments as preferred values, whereas we rule out kinetic PV results owing to possible saturation problems and note in passing that β-NAT is apparently more prone to saturation than α-NAT. The Arrhenius representation for the preferred TO results is:

$$\text{TO Experiments:}\quad \log J_{ev}(H_2O)[\text{molec} \cdot \text{cm}^{-2} \cdot \text{s}^{-1}] = (36.0 \pm 1.3) - \frac{(77.0 \pm 4.9) \times 10^3}{2.303\ \text{RT}} \quad (15)$$

HCl kinetic measurements on α-NAT and β-NAT indicate that HCl does not displace a significant number of HNO_3 molecules from the ice surface upon deposition, but rather that HCl and HNO_3 do not strongly interact with each other in the condensed phase and that HCl evaporates faster. This observation is also supported by the slower rates of evaporation and the correspondingly higher values of the HNO_3 evaporation activation energy on α-NAT and β-NAT, $E_{ev}(HNO_3)$ = (178.0 ± 27.4) and (102.0 ± 8.6) kJ mol^{-1} (see Table 4), respectively,

compared to the activation energy for HCl evaporation on $HCl \bullet 6H_2O$, $E_{ev}(HCl) = (87.0 \pm 17)$ kJ mol^{-1}. This also is consistent with a larger calculated interaction energy of HNO_3 with H_2O ("affinity") in α-NAT compared to β-NAT (Weiss et al., 2016) despite the fact that ΔH_f^0(α-NAT) is less stable by 6.0 ± 20 kJ/mol compared to β-NAT.

A look at Table 5 reveals evaporative lifetimes of various ice particles with respect to H_2O evaporation. Equation (26) and (27) present the rudiments of a very simple layer-by-layer molecular model used to estimate evaporation lifetimes (θ_{tot}) at atmospheric conditions (Alcala et al., 2002; Chiesa and Rossi, 2013):

$$\theta_{tot} = (r/a)N_{ML}/J_{ev}^{rh} \quad (26)$$

$$J_{ev}^{rh} = J_{ev}^{max}(1\text{-}rh/100) \quad (27)$$

with r, a, rh and N_{ML} being the radius of the ice particle, shell thickness, relative humidity in % and the number of molecules cm^{-2} corresponding to one monolayer. J_{ev}^{rh} and J_{ev}^{max} are the evaporation fluxes of H_2O at rh and rh = 0, the latter corresponding to the maximum value of J_{ev} which we calculate following Equation (2) or (8). The salient feature of this simple evaporation model is the linear rate of change of the radius or diameter of the particle, a well- and widely known fact in aerosol physics in which the shrinking or growing size (diameter) of an aerosol particle is linear with time if the rate of evaporation is zero order, that is independent of a concentration term.

Table 5 lists the evaporation life times which are not defined in terms of an e-folding time when dealing with first-order processes. In this example the lifetime is the time span between the cradle and death of the particle, this means from a given diameter 2r and "death" at 2r = 0. The chosen atmospheric conditions correspond to 190 K, rh = 80%, a = 2.5 Å for H_2O and 3.35 Å for all other systems, r = 10 μm and estimated values 6×10^{14}, 3×10^{14} and 1×10^{15} molec cm^{-2} for N_{ML} of HNO_3, HCl and H_2O. It is immediately apparent that there is a large variation of θ_{tot} values for atmospherically relevant conditions which goes into the direction of increasing opportunities for heterogeneous interaction with atmospheric trace gases, even for pure ice (PSC type II). Table 5 is concerned with the most volatile component, namely H_2O.

If we now turn our attention to the least volatile component such as HNO_3 in β-NAT we obtain θ_{tot} = 5.1 d and 33.9 d for 0 and 85% HNO_3 atmospheric saturation, the former being the maximum possible evaporation rate for 0% HNO_3 saturation. The other boundary conditions are 190 K, polar upper tropospheric conditions at 11 km altitude (226.3 mb at 210

K), 1 ppb HNO_3, 10 ppm H_2O corresponding to 85% HNO_3 saturation. This goes to show that laboratory experiments on gas-condensed phase exchange of lower volatility components in atmospheric hydrates are fraught with complications. It follows as a corollary that both HCl, but especially HNO_3 contamination of H_2O ice is bound to persist for all practical atmospheric conditions.

At last it is useful to view the outcome of a recent laboratory experiment dealing with the binary HNO_3/H_2O system monitored using a cryogenic mirror hygrometer (CMH) (Gao et al., 2016) in light of the present kinetic results. In the basic experimental set-up the behavior of the sample CMH exposed to a combined low pressure H_2O/HNO_3 flow is compared to the response of a reference CMH that is located upstream of the HNO_3 source and exposed to the H_2O flow alone, and has been described in detail by Thornberry et al. (2011). Any increase in scattering of the incident monitoring laser beam owing to growth of the polycrystalline ice deposit will be counterbalanced by heating of the mirror to bring back the optical detector signal to a predetermined set point. The typical experimental sequence in Gao et al. (2016) starts by establishing pure ice frost layers on both CMH mirrors at a stable mixing ratio of < 10 ppm after which a continuous flow of HNO_3 was added such that the flow past the sample CMH contained 80-100 ppb HNO_3.

After typically one hour the gradual build-up of a NAT layer on the CMH was accompanied by a temperature increase of the sample CMH to settle around the saturation temperature T_{sat} of NAT at the chosen H_2O and HNO_3 flow rate. An increase of the H_2O flow from 6 to 80 ppm led to ice growth on both mirrors accompanied by an increase of T_{sat} of NAT adjusting to the new H_2O flow rate. Suddenly, the HNO_3 flow was shut off which first led to a rapidly decreasing MS signal for HNO_3 but ending up in an above background signal corresponding to 0.5 to 1.0 ppb HNO_3. The temperature of the sample CMH continued to decrease below T_{sat} of pure ice monitored by the reference CMH suggesting that $P_{eq}(H_2O)$ of the condensate had become larger than that of pure ice. This solid state on the sample CMH was called “second condensate”. The low level of HNO_3 continued to react to repetitive increases (CMH heating) and decreases (CMH cooling) of the H_2O flow in a reproducible manner all the while staying below the level corresponding to T_{sat} of pure ice on the reference CMH. These repetitive H_2O on-off sequences provided additional evidence of the continued evaporation of HNO_3 from the condensate. The response of HNO_3 leaving the condensate undersaturated with respect to NAT is at first sight certainly unexpected based on the results displayed in Figures 2b and 4b. However, if one considers the relatively high mirror temperatures ranging between 207 and

213 K between which the "second condensate" was cycled by way of changing the H_2O flows it suddenly becomes conceivable that $R_{ev}(HNO_3)$ becomes equal to $R_{ev}(H_2O)$ in that temperature range. Linear extrapolation of the absolute rates of evaporation hints at similar magnitude for temperatures exceeding 210 K β - NAT (Figure 4). For α-NAT the temperature at which the evaporation rates of H_2O and HNO_3 become equal is even below 200 K owing to a steeper T-dependence of $R_{ev}(HNO_3)$ in α-NAT (Figure 2 and Table 4). We conclude, that the observed dynamics of the experiment performed by Gao et al. (2016) is entirely consistent with the kinetic results of the present study. However, the results of the Gao et al. (2016) laboratory experiment would certainly be different at lower temperatures more representative of the UT/LS.

Acknowledgements

The authors would like to acknowledge the generous support of this work over the years by the Swiss National Science Foundation (SNSF) in the framework of projects 200020_125204 and 200020_144431/1. We also sincerely thank Mr. Alwin Frei of PSI for graciously granting the permission to perform the experiments in his laboratory and professors Urs Baltensperger and Alexander Wokaun, both of PSI, for unfailing support over the years.

References

Alcala-Jornod, A., van den Bergh, H., and Rossi, M.J.: Can soot particles emitted by airplane exhaust contribute to the formation of aviation contrails and cirrus clouds?, Geophys. Res. Lett. 29, 1820, doi:10.1029/2001GL014115, 2002.

Benson, S.W., "Thermochemical Kinetics", Methods for the Estimation of Thermochemical Data and Rate Parameters", Second Edition, John Wiley and Sons, 1976.

Berland, B.S., Haynes, D.R., Foster, K.L., Tolbert, M.A., George S.M. and Toon, O.B.: Refractive Indices of Amorphous and Crystalline HNO_3/H_2O Films Representative of Polar Stratospheric Clouds, J. Phys. Chem. 98, 4358-4364, 1994.

Biermann, U. M., Crowley J.N., Huthwelker T., Moortgat G. K., Crutzen P. J., and Peter T.: FTIR studies on lifetime prolongation of stratospheric ice particles due to NAT coating, Geophys. Res. Lett., 25(21), 3939–3942, 1998.

Chaix, L., van den Bergh, H., and Rossi, M. J.: Real-Time kinetic measurements of the condensation and evaporation of D_2O molecules on ice at 140 K < T < 220 K, J. Phys. Chem. A, 102(50), 10300–10309, 1998.

Crowley, J.N., Ammann, M., Cox, R.A., Hynes, R.G., Jenkin, M.E., Mellouki, A., Rossi, M.J., Troe, J., and Wallington, T.J.: Evaluated kinetic and photochemical data for atmospheric chemistry: Volume V – heterogeneous reactions on solid substrates, Atmos. Chem. Phys. 10, 9059-9223, 2010.

Chiesa, S., and Rossi, M. J.: The metastable $HCl•6H_2O$ phase – IR spectroscopy, phase transitions and kinetic/thermodynamic properties in the range 170-205 K, Atmos. Chem. Phys., 13(23), 11905–11923, 2013; doi:10.5194/acp-13-11905-2013.

Delval, C., Flückiger, B., and Rossi, M. J.: The rate of water vapor evaporation from ice substrates in the presence of HCl and HBr: implications for the lifetime of atmospheric ice particles, Atmos. Chem. Phys. 3, 1131–1145, 2003.

Delval, C., and Rossi, M. J.: The kinetics of condensation and evaporation of H_2O from pure ice in the range 173-223 K: a quartz crystal microbalance study, Phys. Chem. Chem. Phys., 6: 4665–4676, 2004.

Delval, C., and Rossi, M. J.: Influence of monolayer amounts of HNO_3 on the evaporation rate of H_2O over ice in the range 179 to 208 K: A quartz crystal microbalance study, J. Phys. Chem. A, 109(32), 7151–7165, 2005.

Escribano, R. M., Fernandez-Torre, D., Herrero, V. J., Martin-Llorente, B., Maté, B., Ortega, I. K., and Grothe, H.: The low-frequency Raman and IR spectra of nitric acid hydrates, Vib. Spectrosc., 43, 254–259, 2007.

Fahey, D.W., Gao, R.S., Carslaw, K.S., Kettleborough, J., Popp, P.J., Northway, M.J., Holecek, J.C., Ciciora, S.C., McLaughlin, R.J., Thompson, T.L., Winkler, R.H., Baumgardner, D.G., Gandrud, B., Wennberg, P.O., Dhaniyala, S., McKinney, K., Peter, Th., Salawitch, R.J., Bui, T.P., Elkins, J.W., Webster, C.R., Atlas, E.L., Jost, H., Wilson, J.C., Herman, R.L., Kleinböhl, A., von König, M.: The Detection of Large HNO_3-Containing Particles in the Winter Arctic Stratosphere, Science 291, 1026-1031, 2001.

Friedel, R. A., Shultz, J. L., and Sharkey, A. G.: Mass spectrum of nitric acid, Anal. Chem., 31(6), 1128–1128, 1959.

Gao, R.S., Popp, P.J., Fahey, D.W., Marcy, T.P., Herman, R.L., Weinstock, E.M., Baumgardner, D.G., Garrett, T.J., Rosenlof, K.H., Thompson, T.L., Bui, P.T., Ridley, B.A., Wofsy, S.C., Toon, O.B., Tolbert, M.A., Kärcher, B., Peter, Th., Hudson, P.K., Weinheimer, A.J., Heymsfield, A.J.: Evidence That Nitric Acid Increases Relative Humidity in Low-Temperature Cirrus Clouds, Science 303, 516-520, 2004.

Gao, R.S., Gierczak, T., Thornberry, T.D., Rollins, A.W., Burkholder, J.B., Telg, H., Voigt, C., Peter, T. and Fahey, D.W.: Persistent Water-Nitric Acid Condensate with Saturation Water Vapor Pressure Greater than That of Hexagonal Ice, J. Phys. Chem. A 120, 1431-1440, 2016.

Hamill, P., Turco, R. P., and Toon, O. B.: On the growth of nitric and sulfuric acid aerosol particles under stratospheric conditions. J. Atmos. Chem., 7(3), 287–315, 1988.

Hanson, D. R., and Mauersberger, K.: Laboratory studies of the nitric acid trihydrate: Implications for the south polar stratosphere, Geophys. Res. Lett., 15(8), 855–858, 1988.

Hanson, D. R.: The uptake of HNO_3 onto Ice, NAT and frozen sulfuric acid, Geophys. Res. Lett., 19(20), 2063–2066, 1992.

Herrero, V. J., Ortega, I. K., Maté, B., Martin-Llorente, B., Escribano, R., and H. Grothe: Comment on “Theoretical investigation of the coexistence of α- and β-nitric acid trihydrates

(NAT) molecular conformation" [Chem. Phys. 324 (2006) 210], Chem. Phys., 331, 186–188, 2006.

Höpfner, M., Luo, B.P., Massoli, P., Cairo, F., Spang, R., Snels, M., Di Donfrancesco, G., Stiller, G., von Clarmann, T., Fischer, H., Biermann, U.: Spectroscopic evidence for NAT, STS, and ice in the MIPAS infrared limb emission measurements of poolar stratospheric clouds, Atmos. Chem. Phys., 6, 1201-1219, 2006.

Hynes, R. G., Fernandez, M. A., and Cox, R. A.: Uptake of HNO_3 on water-ice and coadsorption of HNO_3 and HCl in the temperature range 210–235 K, J. Geophys. Res. Atmos., 107(D24), AAC 19–1–AAC 19–11, 2002.

Iannarelli, R., and Rossi, M. J.: H_2O and HCl trace gas kinetics on crystalline HCl hydrates and amorphous HCl/H_2O in the range 170 to 205 K: the HCl/H_2O phase diagram revisited, Atmos. Chem. Phys., 14(10), 5183-5204, 2014.

Iannarelli, R., and Rossi, M. J.: The mid-IR Absorption Cross Sections of α- and β-NAT (HNO_3•$3H_2O$) in the range 170 to 185 K and of metastable NAD (HNO_3•$2H_2O$) in the range 172 to 182 K, J. Geophys. Res. Atmos., 120, 11707-11727, 2015.

Ji, K. and Petit, J.-C., Calorimetric Identification of a new Nitric Acid Hydrate able to play a Role in the heterogeneous Chemistry of the Stratosphere, Compt. Rend. Acad. Sciences Ser II, 316(12), 1743-1748, 1993.

Koehler, B. G., Middlebrook, A. M., and Tolbert, M. A.: Characterization of model polar stratospheric cloud films using Fourier transform infrared spectroscopy and temperature programmed desorption, J. Geophys. Res., 97(D8), 8065–8074, 1992.

Kuhs, W. F., Sippel, C., Falenty, A., and Hansen, T. C.: Extent and relevance of stacking disorder in "ice I_c", PNAS, 109(52), 21259– 21264, 2012.

Marti, J., and Mauersberger, K.: A survey and new measurements of ice vapor pressure at temperatures between 170 and 250 K, Geophys. Res. Lett., 20, 363–366, 1993.

Martin-Llorente, B., Fernandez-Torre, D., Herrero, V. J., Ortega, I. K., Escribano, R., and Maté, B.: Vibrational spectra of crystalline hydrates of atmospheric relevance: Bands of hydrated protons, Chem. Phys. Lett., 427, 300–304, 2006.

Mauersberger, K., and Krankowsky, D.: Vapor pressure above ice at temperatures below 170 K, Geophys. Res. Lett., 30(3), 1121, 2003.

McElroy, M. B., Salawitch, R. J., and Wofsy, S. C.: Antarctic O_3: Chemical mechanisms for the spring decrease. Geophys. Res. Lett., 13(12), 1296–1299, 1986.

McNeill, V. F., Loerting, T., Geiger, F. M., Trout, B. L., and Molina, M. J.: Hydrogen chloride-induced surface disordering on ice. PNAS, 103(25), 9422–9427, 2006.

McNeill, V. F., Geiger, F. M., Loerting, T., Trout, B. L., Molina, L. T., and Molina, M. J.: Interaction of hydrogen chloride with ice surfaces: the effects of grain size, surface roughness, and surface disorder. J. Phys. Chem. A, 111(28), 6274–6284, 2007.

Middlebrook, A. M., Koehler, B. G., McNeill, L. S., and Tolbert, M. A.: Formation of model polar stratospheric cloud films, Geophys. Res. Lett., 19(24), 2417–2420, 1992.

Middlebrook, A.M., Tolbert, M.A., and Drdla, K.: Evaporation studies of model polar stratospheric cloud films, Geophys. Res. Lett. 23, 2145-2148, 1996.

Molina, L. T., Molina M. J., Stachnik, R. A., and Tom, R. D.: An upper limit to the rate of the HCl + $ClONO_2$ reaction, J. Phys. Chem. 89, 3779-3781, 1985.

Molina, M. J., Tso, T. L., Molina, L. T., and Wang, F. C. Y.: Antarctic stratospheric chemistry of chlorine nitrate, hydrogen chloride and ice: release of active chlorine, Science 238, 1253-1257, 1987.

Molina, M. J.: The Probable Role of Stratospheric 'Ice' Clouds: Heterogeneous Chemistry of the Ozone Hole, in "The Chemistry of the Atmosphere: Its Impact on Global Change", Blackwell Scientific Publications, London, ch. 3, pp 27- 38, 1994.

Moussa, S. G., Kuo, M. H., and McNeill, V. F.: Nitric acid-induced surface disordering on ice, Phys. Chem. Chem. Phys., 15, 10989–10995, 2013.

Ortega, I. K., Escribano, R., Fernandez, D., Herrero, V. J., Maté, B., Medialdea, A., and Moreno, M. A.: The structure and vibrational frequencies of crystalline nitric acid, Chem. Phys. Lett., 378, 218–223, 2003.

Ortega, I. K., Maté, B., Moreno, M. A., Herrero, V. J., and Escribano, R.: Infrared spectra of nitric acid trihydrate (β-NAT): A comparison of available optical constants and implication for the detection of polar stratospheric clouds (PSC's), Geophys. Res. Lett., 33 L19816, 2006.

Peter, Th.: Microphysics and heterogeneous chemistry of Polar Stratospheric Clouds, Annu. Rev. Phys. Chem. 48, 785-822, 1997.

Pratte P., van den Bergh H., and Rossi, M. J.: The kinetics of H_2O vapor condensation and evaporation on different types of ice in the range 130-210 K, J. Phys. Chem A, 110(9), 3042–3058, 2006.

Reinhardt, H., Fida, M., and Zellner, R.: DRIFTS-studies of the interactions of HNO_3 with ice and HCl (HNO_3)-hydrate surfaces at temperatures around 165 K, J. Mol. Struct., 661–662, 567–577, 2003.

Ritzhaupt, G., and Devlin, J. P.: Infrared spectra of nitric and hydrochloric acid hydrate thin films, J. Phys. Chem. 95, 90-95, 1991.

Schreiner, J., Voigt, C., Kohlmann, A., Arnold F., Mauersberger, K. and Larsen, Niels, Chemical Analysis of Polöar Stratospheric Cloud Particles, Science, 283, 968-970, 1999.

Schreiner, J., Voigt, C., Weisser, C., Kohlmann, A., Mauersberger, K., Deshler, T., Kröger, C., Rosen, J., Kjome, N., Larsen, N., Adriani, A., Cairo, F., Di Donfrancesco, G., Ovarlez, J., Ovarlez, H., and Dörnbrack, A.: Chemical, microphysical, and optical properties of polar stratospheric clouds, J. Geophys. Res., 108(D5), 8313, 2003.

Solomon, S., Garcia, R.R., Rowland, F.S., and Wuebbles, D.J.: On the depletion of Antarctic ozone, Nature 321, 755-758, 1986.

Solomon, S.: Progress towards a quantitative understanding of Antarctic ozone depletion, Nature 347, 347-354, 1990.

Thornberry, T.D., Gierczak, T., Gao, R.S., Vömel, H., Watts, L.A., Burkholder, J.B., Fahey, D.W.: Laboratory evaluation of the effect of nitric acid uptake on frost point hygrometer performance, Atmos. Meas. Tech. 4, 289-296, 2011.

Tolbert, M. A., and Middlebrook, A. M.: Fourier transform infrared studies of model polar stratospheric cloud surfaces: Growth and evaporation of ice and nitric acid/ice, J. Geophys. Res., 95(D13), 22423–22431, 1990.

Tolbert, M. A., Koehler, B. G., and Middlebrook, A. M.: Spectroscopic studies of model polar stratospheric cloud films, Spectrochim. Acta Part A: Mol. Spectrosc., 48(9), 1303–1313, 1992.

Toon, O.B., Tolbert, M.A., Koehler, B.G., Middlebrook, A.M. and J. Jordan, J.: Infrared optical constants of H_2O ice, amorphous nitric acid solutions, and nitric acid hydrates, Geophys. Res. 99(D12), 25631-25654 (1994).

1172 Tso, T.-L., and Leu, M.-T.: Quantitative analysis of the infrared absorptivities of nitric acid
1173 ices existing in polar stratospheric clouds, Anal. Sci., 12, 615–622, 1996.

1174 Voigt, C., Schreiner, J., Kohlmann, A., Zink, P., Mauersberger, K., Larsen, N., Deshler, T.,
1175 Kröger, C., Rosen, J., Adriani, A., Cairo, F., Di Donfrancesco, G., Viterbini, M., Ovarlez, J.,
1176 Ovarlez, H., David, C., and Dörnbrack A.: Nitric Acid Trihydrate (NAT) in Polar
1177 Stratospheric Clouds, Science, 290, 1756-1758, 2000.

1178 Voigt, C., Schreiner, J., Kohlmann, A., Zink, P., Mauersberger, K., Larsen, N., Deshler, T.,
1179 Kröger, C., Rosen, J., Adriani, A., Cairo, F., Di Donfrancesco, G., Viterbini, M., Ovarlez, J.,
1180 Ovarlez, H., David, C. and Dörnbrack, A., Science 290, 1756-1758, 2000.

1181 Voigt, C., Schlager, H., Luo, B.P., Dörnbrack, A., Roiger, A., Stock, P., Curtius, J., Vössing,
1182 H., Borrmann, S., Davies, S., Konopka, P., Schiller, C., Shur, G. and Peter, T.: Nitric Acid
1183 Trihydrate (NAT) formation at low NAT supersaturation in Polar Stratospheric Clouds
1184 (PSC's), Atmos. Chem. Phys., 5, 1371-1380, 2005.

1185 Warshawsky, M.S., Zondlo, M.A., and Tolbert, M.A.: Impact of nitric acid on ice evaporation
1186 rates, Geophys. Res. Lett. 26, 823-826, 1999.

1187 Weiss, F., Kubel, F., Gálvez, O., Hoelzel, M., Parker, S. F., Baloh, P., Iannarelli, R., Rossi,
1188 M. J., and Grothe, H.: Metastable Nitric Acid Trihydrate in Ice Clouds, Angew. Chemie I.E.
1189 55, 3276-3280, 2016, doi: 10.1002/anie.201510841.

1190 Wooldridge, P. J., Zhang, R., and Molina, M. J.: Phase equilibria of H_2SO_4, HNO_3, and HCl
1191 hydrates and the composition of polar stratospheric clouds, J. Geophys. Res. Atmos.,
1192 100(D1), 1389–1396, 1995.

1193 Zondlo, M. A., Barone, S. B., and Tolbert, M. A.: Condensed-phase products in
1194 heterogeneous reactions: N_2O_5, $ClONO_2$, and HNO_3 reacting on ice films at 185 K, J. Phys.
1195 Chem. A, 102, 5735–5748, 1998.

1196 Zondlo, M.A., Hudson, P.K., Prenni, A.J., and Tolbert, M.A.: Chemistry and microphysics of
1197 polar stratospheric clouds and cirrus clouds, Ann. Rev. Phys. Chem. 51, 473-499, 2000.
1198

1199 Table 1: Characteristic parameters of the used Stirred Flow Reactor (SFR).

Reactor volume (upper chamber)	$\mathbf{V_R}$ = 2036 cm^3		
MS (lower) chamber	$\mathbf{V_{MS}}$ = 1750 cm^3		
Reactor internal surface	$\mathbf{S_W}$ = 1885 cm^2		
H_2O calibrated volume – inlet line	$\mathbf{V_{water}}$ = 62 cm^3		
HNO_3 calibrated volume – inlet line	$\mathbf{V_{acid}}$ = 20 cm^3		
Si support area (one side)	$\mathbf{A_{Si}}$ = 0.99 cm^2		
Surface to Volume ratio	$\mathbf{2\ A_{Si}/V_R}$ = 0.9725×10^{-4} cm^{-1}		
Reactor wall temperature	$\mathbf{T_w}$ = 315 K		
Conversion of evaporation rate and flux	$\mathbf{R_{ev} \cdot V_R = 2 \cdot A_{Si} \cdot J_{ev}}$		
	HNO_3	**H_2O**	**HCl**
Base Peak Signal MS [m/z]	46	18	36
MS Calibration Factor $\mathbf{C^X}$ [$molec^{-1}$ s A]	4.53×10^{-25}	6.65×10^{-25}	1.30×10^{-25}
Escape rate constant $k_{esc}^{S} = C^{S}\sqrt{\frac{T}{M}}$ (small orifice) [s^{-1}]	0.0913	0.1710	0.1213
$k_{esc}^{M} = C^{M}\sqrt{\frac{T}{M}}$ (both orifices) [s^{-1}]	0.4331	0.8102	0.5729
Gas-surface collision frequency at 315 K, one side [s^{-1}] [(a)] $\omega = \frac{\bar{c}}{4V}\cdot A_{Si} = \sqrt{\frac{8\,R\,T}{\pi\,M}}\cdot\frac{A_{Si}}{4V}$	3.95	7.39	5.22

1200 [(a)] M in kg; A_{Si} in m^2; V in m^3; R = 8.314 J K^{-1} mol^{-1}. "One side" corresponds to front or rear side of Si-window.
1201 In order to calculate the accommodation coefficient α using equation (3) we have used 2ω as the total collision
1202 frequency for both sides of the Si-window.
1203

Table 2: Fit parameters of the Langmuir adsorption isotherms for H_2O, HNO_3 and HCl interaction with the internal stainless steel (SS304) surfaces of the SFR.

Adsorbed Gas (Additional Gas) [(a)]	$\mathbf{K_L}$ $[\times 10^{-14}]$ [(b)]	$\mathbf{N_{TOT}}$ $[\times 10^{17}]$ [(c)]	$\mathbf{N_{MAX}}$ $[\times 10^{14}]$ [(d)]	$\boldsymbol{\alpha_w}$ $[\times 10^{-6}]$ [(e)]
H_2O	3.18 ± 0.38	7.03 ± 0.42	3.73 ± 0.22	6.19 ± 0.08
H_2O (HCl, $F_{in} = 8\times10^{14}$)	4.67 ± 0.39	8.38 ± 0.29	4.45 ± 0.15	–
HNO_3	1.10 ± 0.16	93 ± 11	49 ± 6	2.92 ± 0.10
HNO_3 (H_2O, $F_{in} = 2\text{-}3\times10^{15}$)	1.61 ± 0.40	76 ± 15	40 ± 8	–
HNO_3 (average values)	1.28 ± 0.17	84 ± 8	45 ± 4	–
HCl	437 ± 21	5.06 ±0.06	2.68 ± 0.03	16.9 ± 0.3
HCl (H_2O, $F_{in} = 6\times10^{15}$)	63.1 ± 4.9	4.85 ± 0.07	2.57 ± 0.04	–
HCl (H_2O, $F_{in} = 3\times10^{15}$)	64.6 ± 6.3	3.79 ± 0.09	2.01 ± 0.04	–

[(a)] F_{in} is the flow rate of the additional gas in molec s^{-1}.
[(b)] K_L is the Langmuir adsorption equilibrium constant in cm^3 $molec^{-1}$.
[(c)] N_{TOT} is the total number of adsorbed molecules onto the internal surfaces, reported is the saturation value for total internal surface (1885 cm^2) of SFR.
[(d)] N_{MAX} is the adsorption site density in molec cm^{-2}.
[(e)] α_w is the reactor wall accommodation coefficient.

Table 3: Peak Positions in cm^{-1} in the mid-IR of HNO_3 and HNO_3/HCl Hydrates[a].

α-NAT/HCl this work	**β-NAT/HCl this work**	**α-NAT/ice Iannarelli et al., 2015**	**β-NAT/ice Iannarelli et al., 2015**	**HCl/H_2O am Iannarelli et al., 2014**
3430 (sh)		3430		
3354 (sh)	*3360*		3377	3360
3233[b]	3227[b]	3233[b]	3233[b]	3236[b]
1767[c,d]	1850[c]	1760[c]	1850[c]	1730[c]
1828[c,d], *1625-1560*[c,d]				1639[c]
1375	1378	1385	1378	
1328	1339		1339	
1196	*1198*			

[a] Values in italics indicate significant changes in the spectrum upon addition of HCl to α- or β-NAT.
[b] The vibration on the third entry invariably corresponds to ν_3 (antisymmetric stretch) H-O-H in H_2O ice.
[c] Broad band. The estimated uncertainty in the peak position is ± 7.5 compared to the usual ± 2 cm^{-1}.
[d] With increasing HCl content broad band at 1767 cm^{-1} splits into two bands at 1828 and 1525-1650 cm^{-1}.

Table 4: Synopsis of thermodynamic (P_{eq}) and kinetic (J_{ev}) parameters of the Arrhenius and van 't Hoff representation of data from Figure 2, Figure 4, Figure 8 and Figure 9.

			$\mathbf{J_{ev}}$ [a]		$\mathbf{P_{eq}}$ [b]	
			$\mathbf{E_{ev}}$	**A**	$\mathbf{\Delta H^0_{ev}}$	$\mathbf{\Delta S/_R}$
Sample	**Gas**	**Exp.**				
α-NAT	H_2O	TO	75.3 ± 9.9	35.9 ± 2.8	70.3 ± 14.1	15.2 ± 4.0
		PV	3.5 ± 4.2	15.1 ± 1.2	56.5 ± 5.1	11.8 ± 1.5
	HNO_3	TO	178.0 ± 27.4	62.3 ± 7.8	128.6 ± 42.4	29.3 ± 12.0
	HCl	PV	78.3 ± 19.2	34.8 ± 5.3	78.4 ± 11.4	15.7 ± 3.2
β-NAT	H_2O	TO	77.0 ± 4.9	36.0 ± 1.3	76.7 ± 17.7	16.7 ± 4.9
		PV	52.1 ± 2.4	28.7 ± 0.7	75.5 ± 11.1	16.7 ± 3.0
	HNO_3	TO	102.0 ± 8.6	40.6 ± 2.4	96.5 ± 12.0	19.8 ± 3.3
	HCl	PV	56.7 ± 4.6	28.6 ± 1.3	69.6 ± 5.8	13.3 ± 1.6

[a] for gas X, R = 8.314 J K^{-1} mol^{-1}: $\log J_{ev}(X)[\text{molec} \cdot \text{cm}^{-2} \cdot \text{s}^{-1}] = A - \frac{E_{ev} \times 10^3}{2.303\ RT}$

[b] for gas X, R = 8.314 J K^{-1} mol^{-1}: $\log P_{eq}(X)[\text{Torr}] = \frac{\Delta S}{R} - \frac{\mathbf{\Delta H^0_{ev}} \times 10^3}{2.303\ RT}$

1231 Table 5: Atmospheric Lifetimes of various 20 μm diameter Ice Particles at 190 K calculated
1232 using the measured absolute rate of H_2O evaporation of corresponding ice particle[a]

Molecular System	**Evaporation Flux J_{ev}(M) (molecule cm^{-2} s^{-1})**	**Lifetime θ/h**	**Dopant Dose/ML (molecular monolayer)**
H_2O	2.1×10^{16}	2.6	pure
HCl/H_2O	5.1×10^{15} 1.4×10^{15}	10.9 39.7	< 3 ML 23 ML
HBr/H_2O	2.1×10^{15}	26.5	< 3 ML
α-NAT/H_2O	1.8×10^{15}	23.1	pure
β-NAT/H_2O	6.0×10^{14}	69.4	pure

1233 [a] Conditions: T= 190 K, rh = 80%, a corresponds to experimentally measured interlayer distance (XRD), a=2.5
1234 and 3.35 Å for H_2O, HCl-, HBr-H_2O and NAT, resp., r=10 μm ice particle, ML for HNO_3, HCl, H_2O is 6 x 10^{14},
1235 3 x 10^{14}, 1 x 10^{15}, respectively.

1236

1237

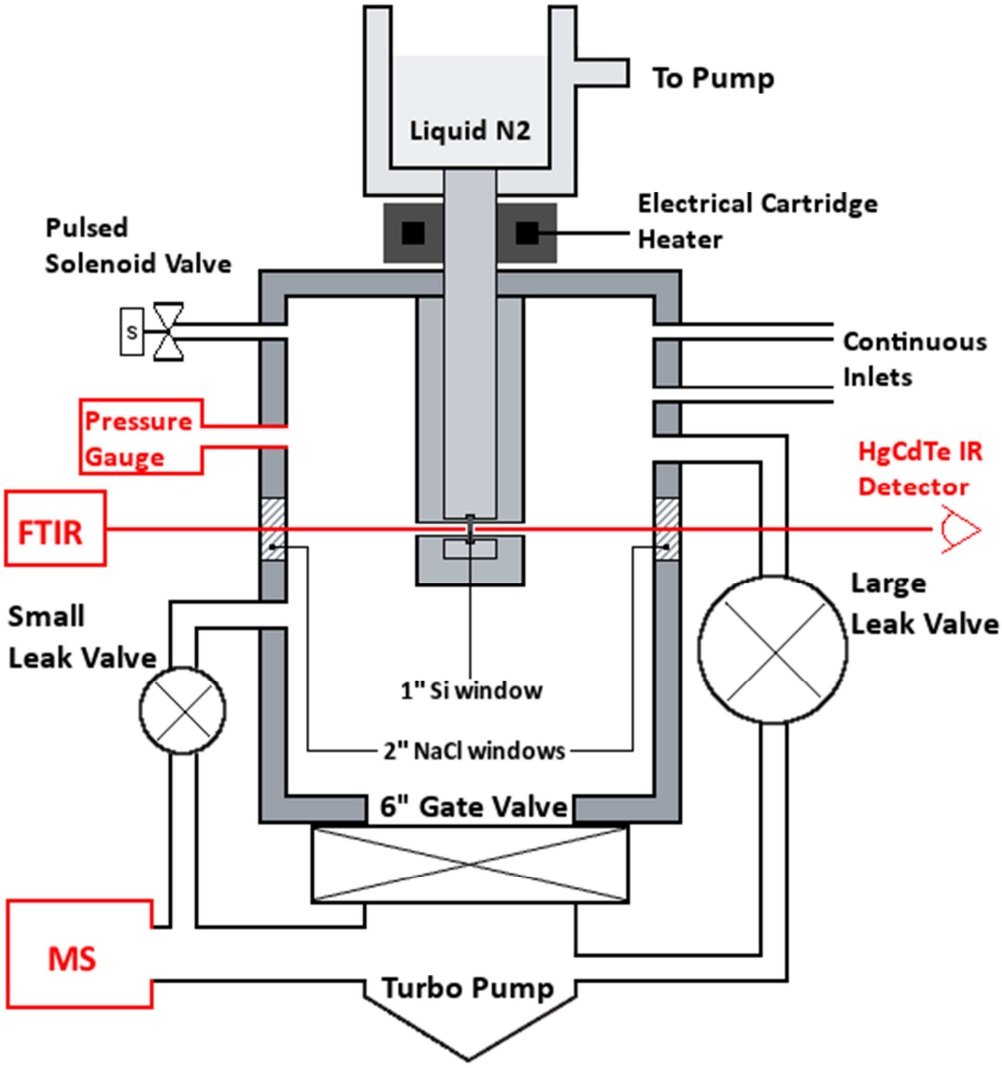

Figure 1: Schematic drawing of the reactor used in this work. The diagnostic tools are highlighted in red and important parameters are listed in Table 1 and Table 2. The ice film is deposited on both sides of the 1" diameter Si window (black vertical symbol hanging from cryostat inside reaction vessel).

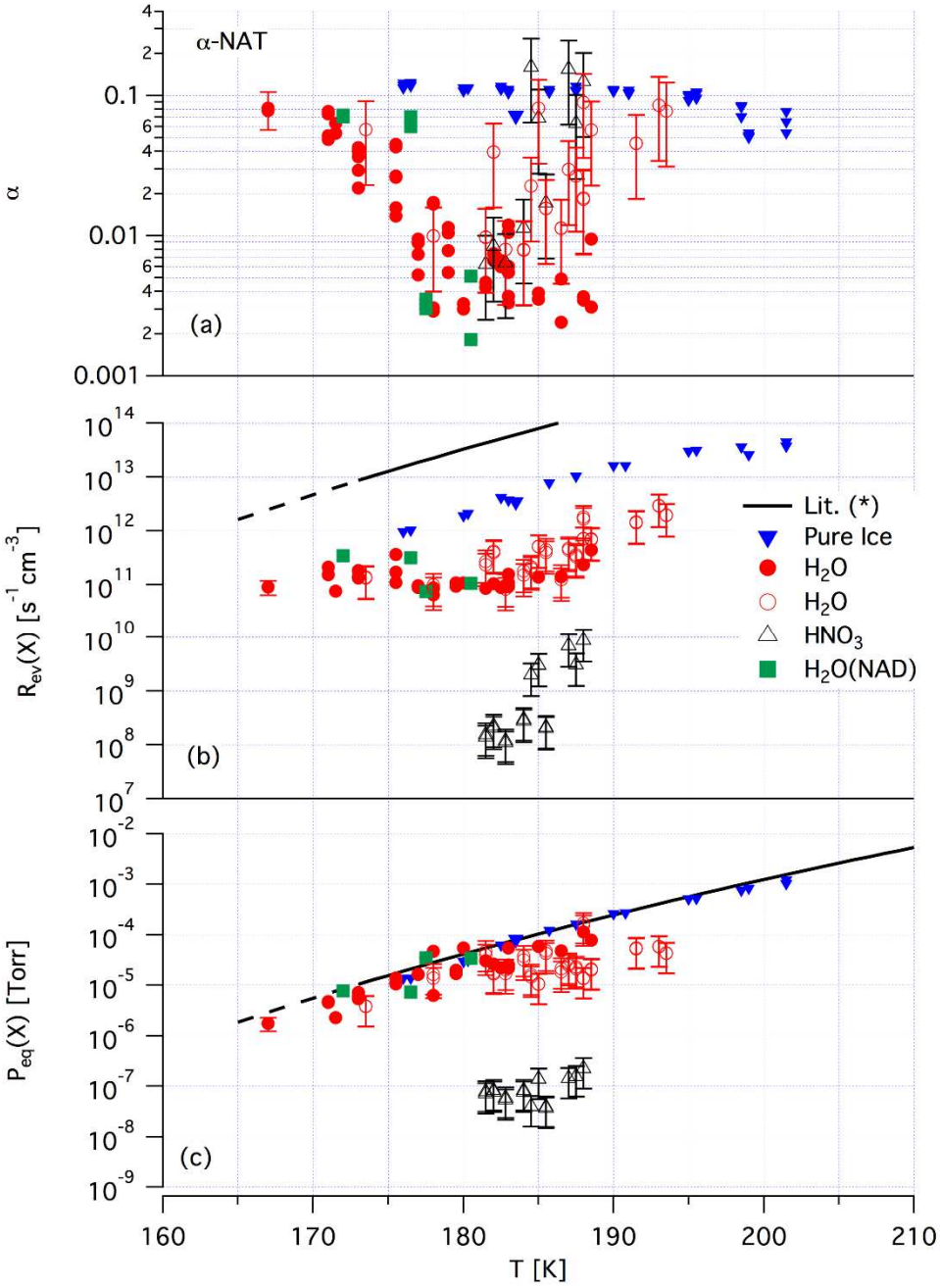

Figure 2: Synopsis of kinetic results for α-NAT and NAD using H_2O as a probe gas in PV experiments and H_2O and HNO_3 in two-orifice (TO) experiments. Full symbols represent PV experiments and empty symbols represent TO experiments. The different symbols are coded in panel b. The calculated relative error for PV experiments is 30% whereas for TO experiments we estimate a relative error of 60%. Examples of the amplitude of the errors are reported for selected points. The black line shows results from Marti and Mauersberger (1993) with $R_{ev}(H_2O)$ of pure ice calculated for the system in use using $\alpha = 1$.

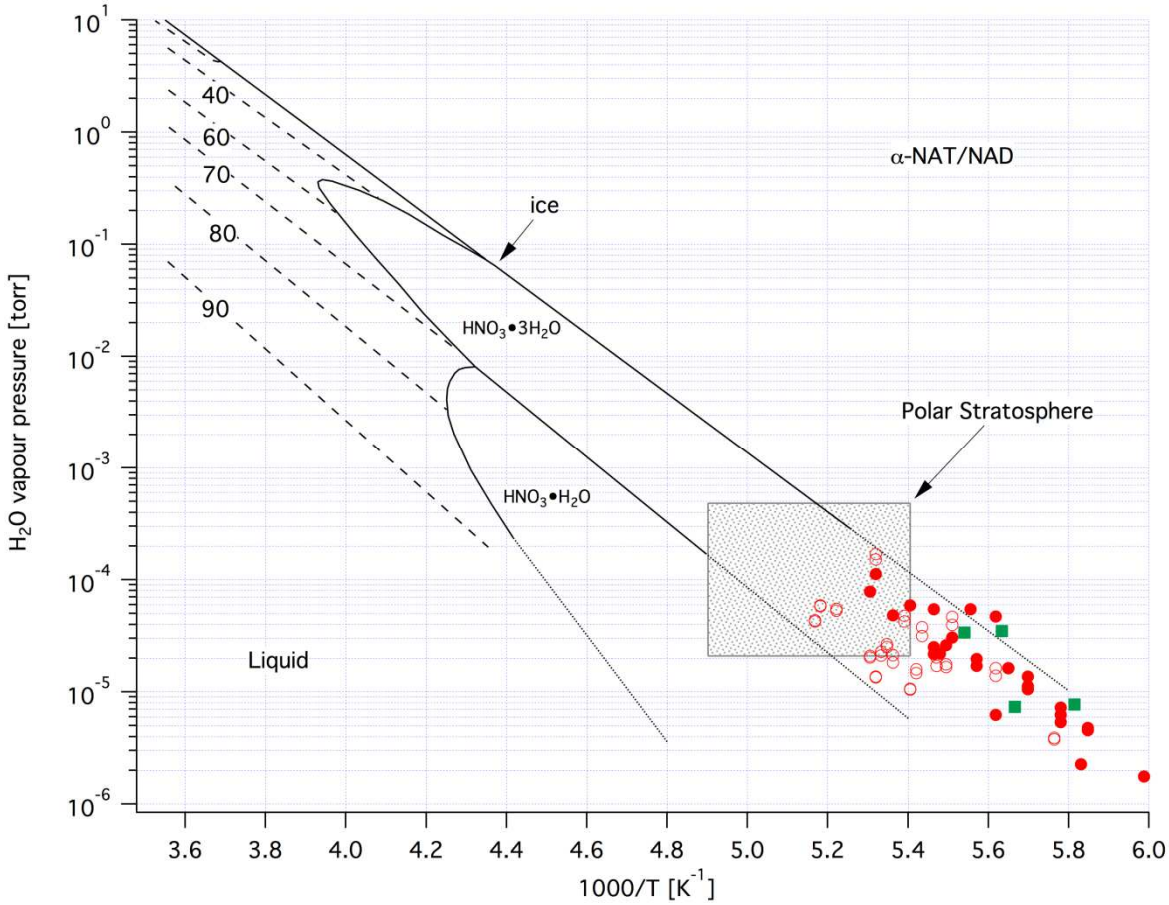

Figure 3: Binary phase diagram of the HNO_3/H_2O system reconstructed from McElroy et al. (1986); Hamill et al. (1988); Molina (1994). The full symbols represent calculated values of $P_{eq}(H_2O)$ for α-NAT and NAD using the kinetic data of PV experiments. Empty circles represent calculated values of $P_{eq}(H_2O)$ for α-NAT using the kinetic data of two-orifice (TO) experiments. The solid lines represent the coexistence conditions for two phases and the dashed lines represent vapor pressures of liquids with composition given as % (w/w) of HNO_3. The shaded gray represents polar stratospheric conditions.

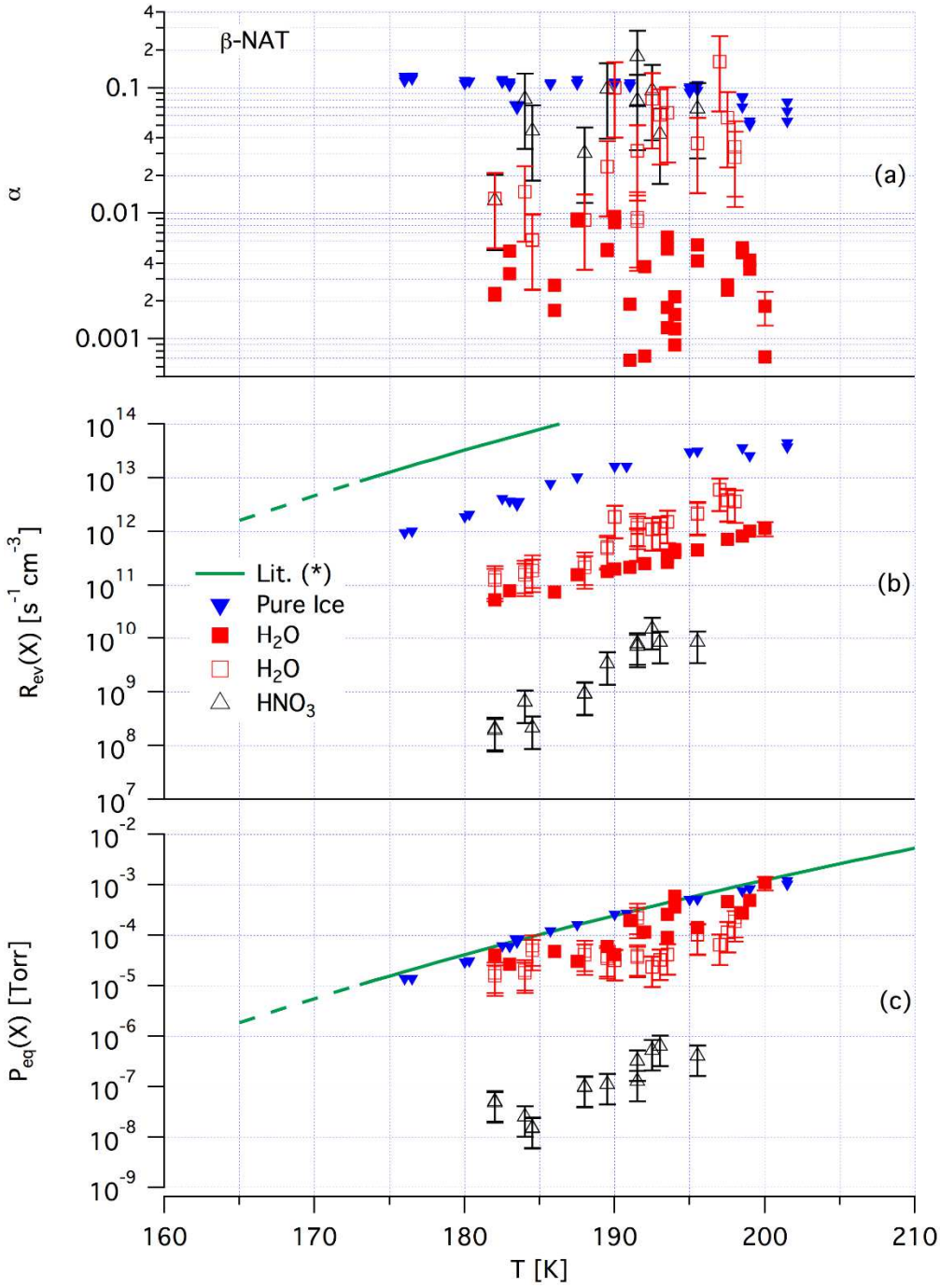

Figure 4: Synopsis of kinetic results for β-NAT using H_2O as a probe gas in PV experiments and H_2O and HNO_3 in two-orifice experiments. Full symbols represent PV experiments and empty symbols represent TO experiments. The different symbols are coded in panel b. The calculated relative error for PV experiments is 30% whereas for TO experiments we estimate a relative error of 60%. Examples of the amplitude of the errors are reported for selected points. The green line shows results from Marti and Mauersberger (1993).

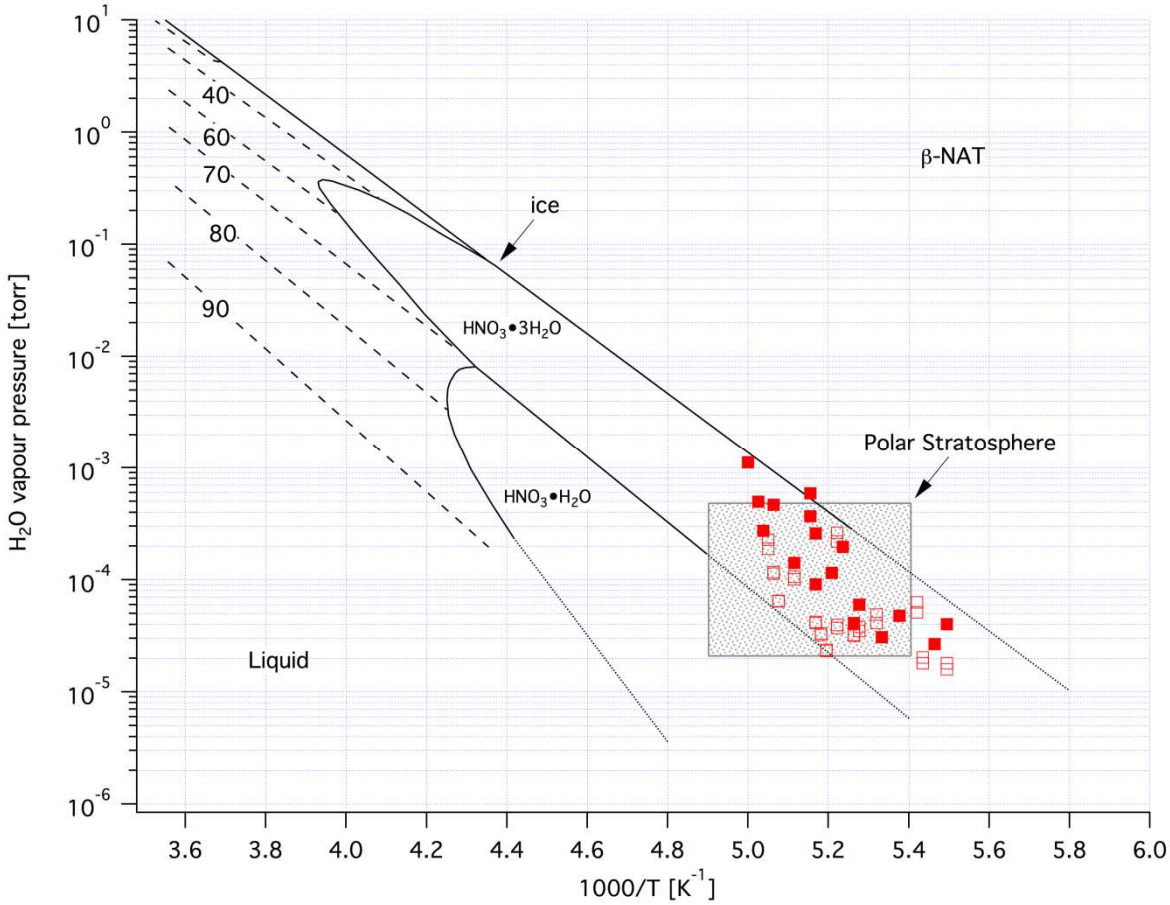

Figure 5: Binary phase diagram of the HNO_3/H_2O system reconstructed from McElroy et al. (1986); Hamill et al. (1988); Molina (1994). The full symbols represent calculated values of $P_{eq}(H_2O)$ for β-NAT using the kinetic data of PV experiments. Empty circles represent calculated values of $P_{eq}(H_2O)$ using the kinetic data of TO (Two-Orifice) experiments. The solid lines represent the coexistence conditions for two phases and the dashed lines represent vapor pressures of liquids with composition given as % (w/w) of HNO_3. The shaded gray represents polar stratospheric conditions.

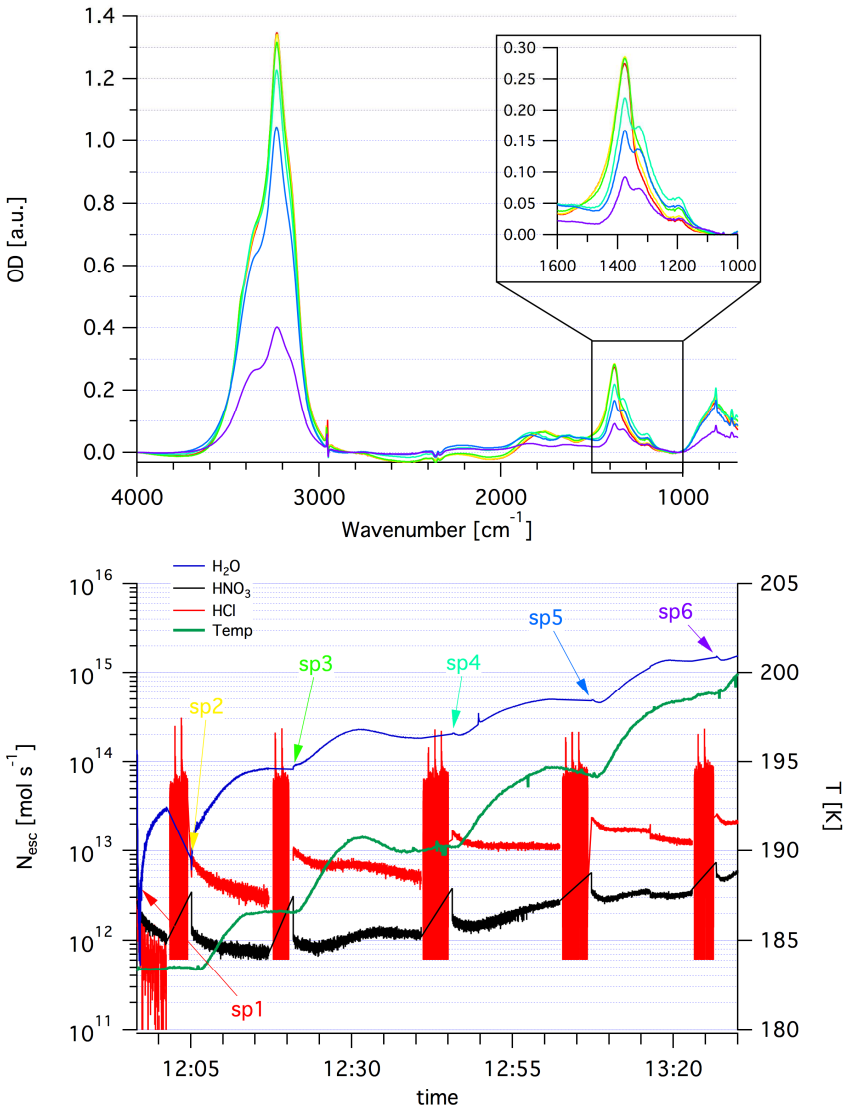

Figure 6: Repetitive PV (Pulsed Valve) deposition experiment of HCl on an α-NAT/ice substrate under SFR conditions followed by MS (lower panel) and FTIR transmission across the thin film (upper panel) as a function of time. In the lower panel the temperature is displayed as the green trace, the red MS signal represents HCl at m/e 36 amu with the pulsed forcing recognizable as single peaks (12) on top of the red columns. The individual HCl doses correspond to approximately (4-5)×10^{16} molecule per pulse resulting in a total dose of 3×10^{17} molecules. The blue and black traces represent the response of H_2O (m/e 18 amu) and HNO_3 (m/e 46 amu) as a function of time (temperature) and HCl forcing. The upper trace displays FTIR transmission spectra at selected times indicated in the lower panel through color coding. The principal peak positions are listed in Table 3 and the changes are discussed in the text.

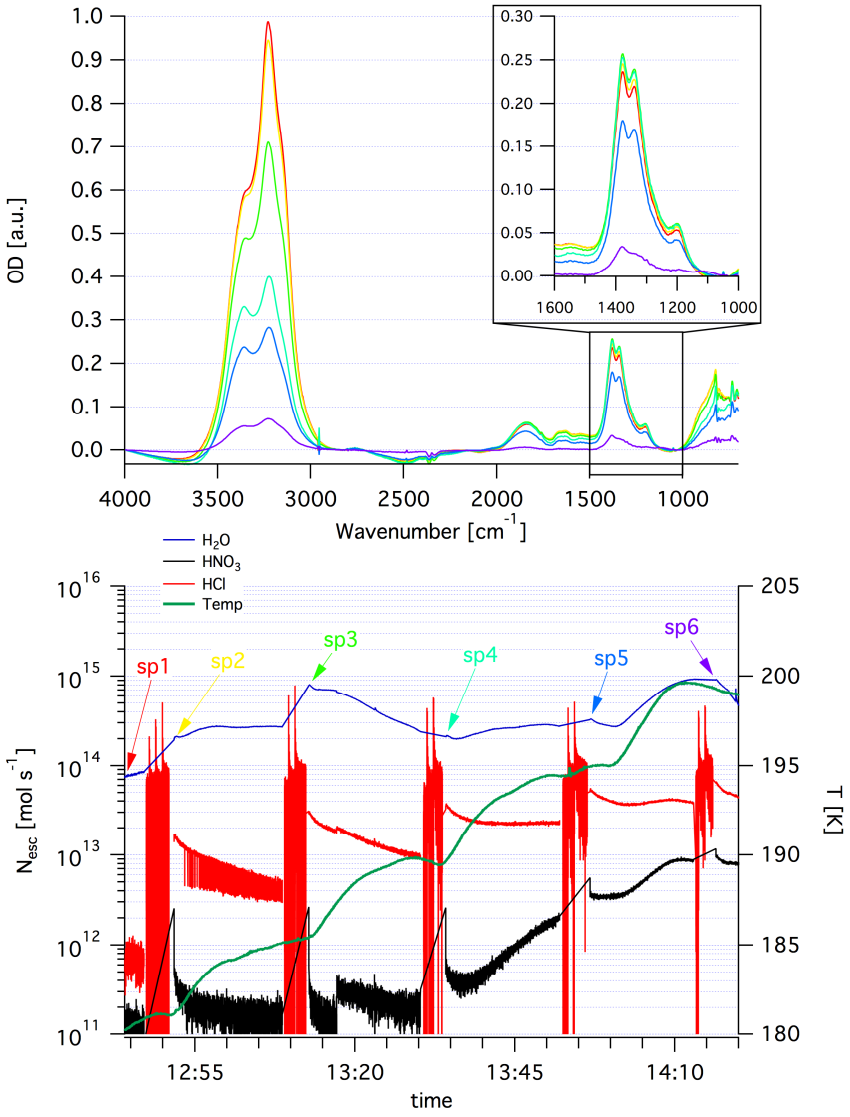

Figure 7: Repetitive PV (Pulsed Valve) deposition experiment of HCl on an β-NAT/ice substrate under SFR conditions followed by MS (lower panel) and FTIR transmission across the thin film (upper panel) as a function of time. In the lower panel the temperature is displayed as the green trace, the red MS signal represents HCl at m/e 36 amu with the pulsed forcing recognizable as single peaks (11) on top of the red columns. The individual HCl doses correspond to approximately (6-7)×10^{16} molecule per pulse resulting in a total dose of 4×10^{17} molecules. The blue and black traces represent the response of H_2O (m/e 18 amu) and HNO_3 (m/e 46 amu) as a function of time (temperature) and HCl forcing. The upper trace displays FTIR transmission spectra at selected times indicated in the lower panel through color coding. The principal peak positions are listed in Table 3 and the changes are discussed in the text.

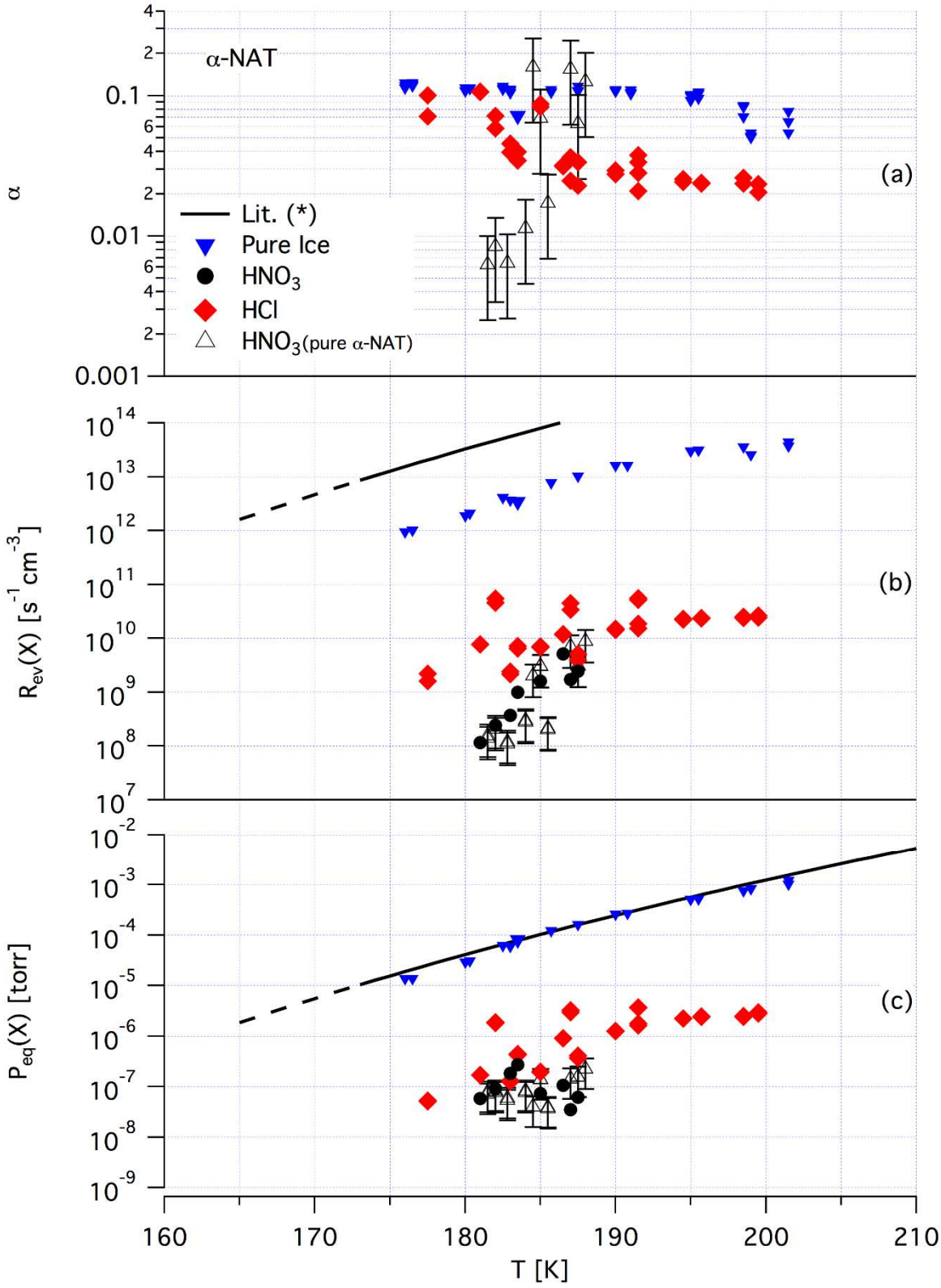

Figure 8: Synopsis of kinetic results for α-NAT using HCl as a probe gas in PV experiments. The used symbols are coded in the upper panel. The calculated relative error for PV experiments is 30%. The black line shows results from Marti and Mauersberger (1993).

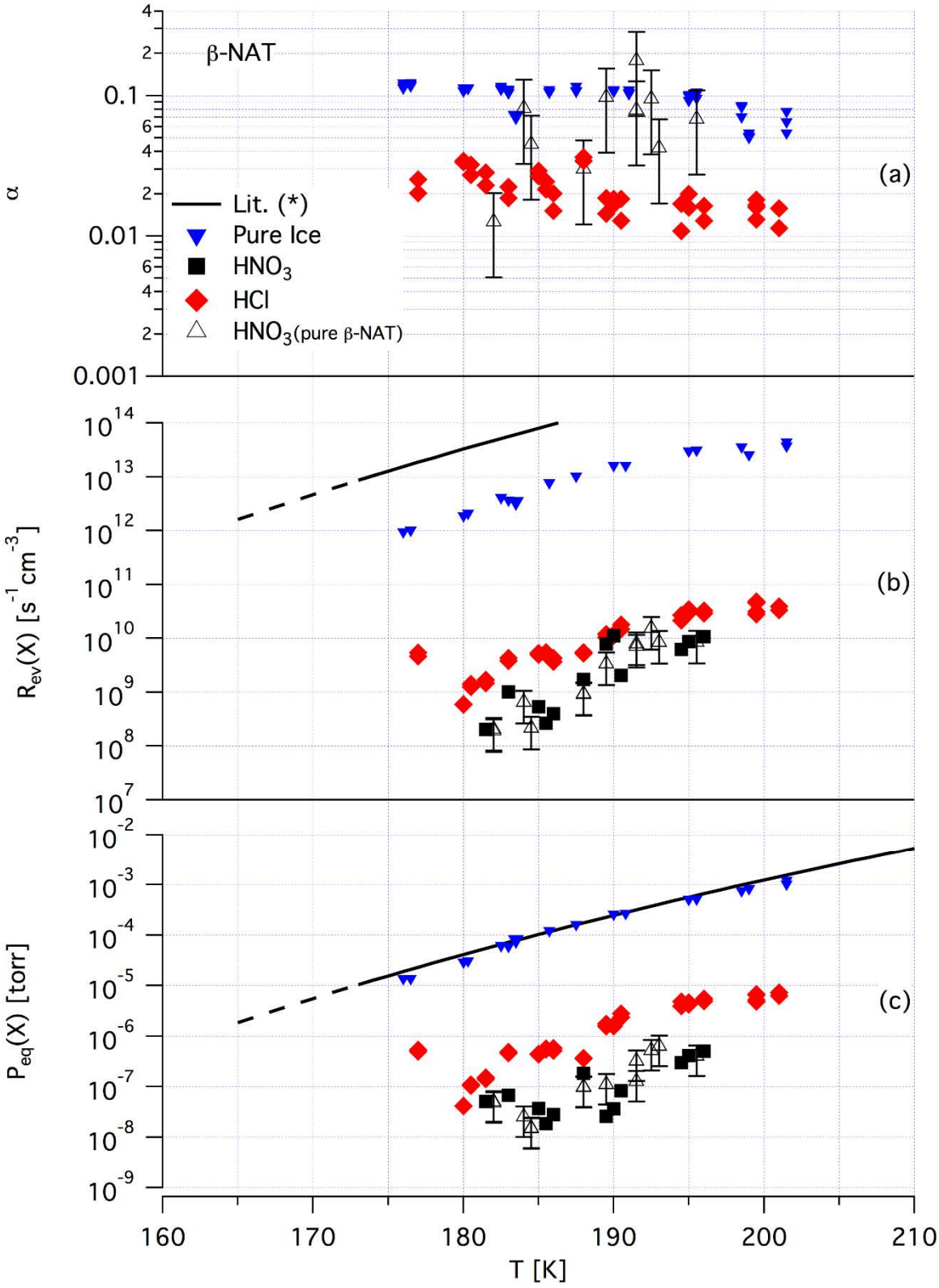

1304

1305 Figure 9: Synopsis of kinetic results for β-NAT using HCl as a probe gas in PV experiments.
1306 The used symbols are coded in the upper panel. The calculated relative error for PV
1307 experiments is 30%. The black line shows results from Marti and Mauersberger (1993).

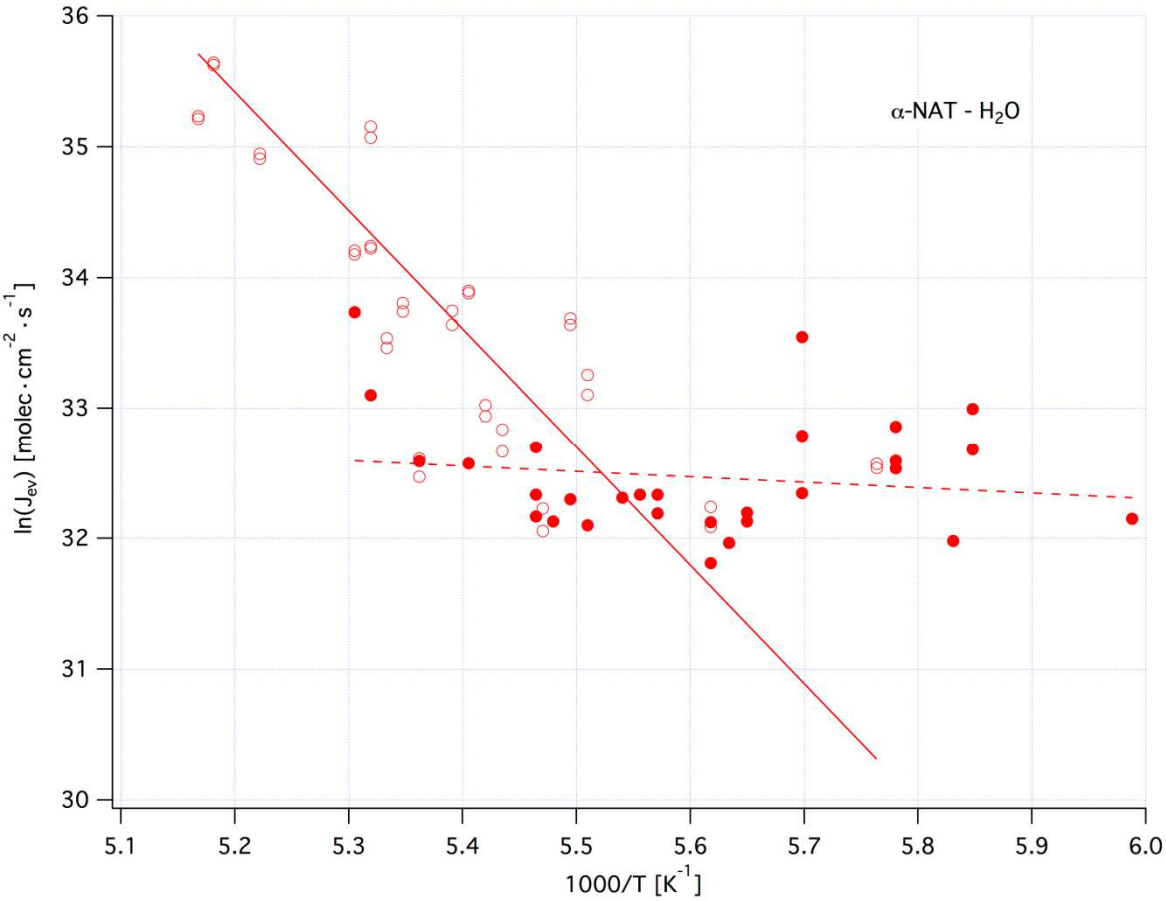

Figure 10: Arrhenius plot of $J_{ev}(H_2O)$ for α-NAT. Full and empty red circles represent results of PV and TO experiments, respectively. Data are taken from Figure 2b and the equations for the linear fits may be found in the text.

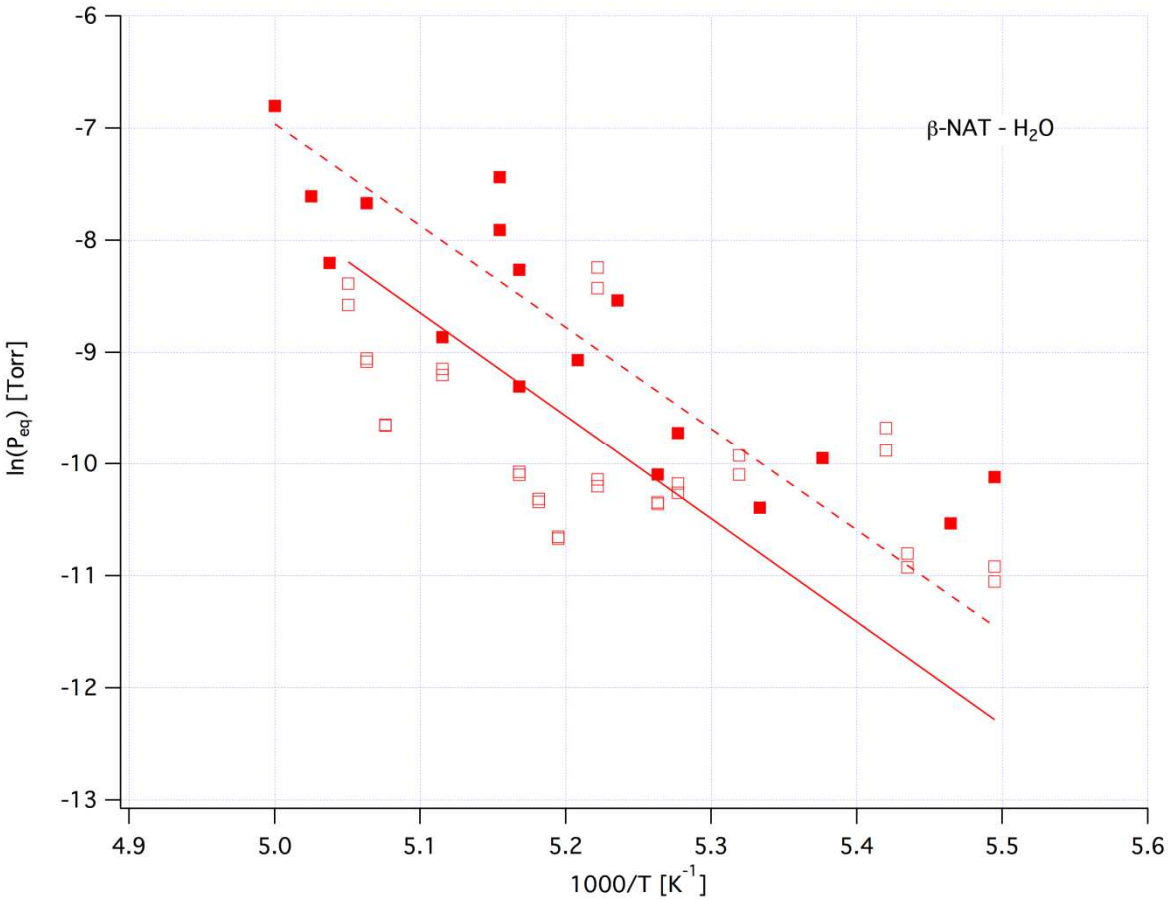

Figure 11: van 't Hoff plot of $P_{eq}(H_2O)$ for β-NAT data displayed in Figure 4c. Full and empty red squares represent results of PV and TO experiments, respectively. The equations for the linear fits may be found in the text.

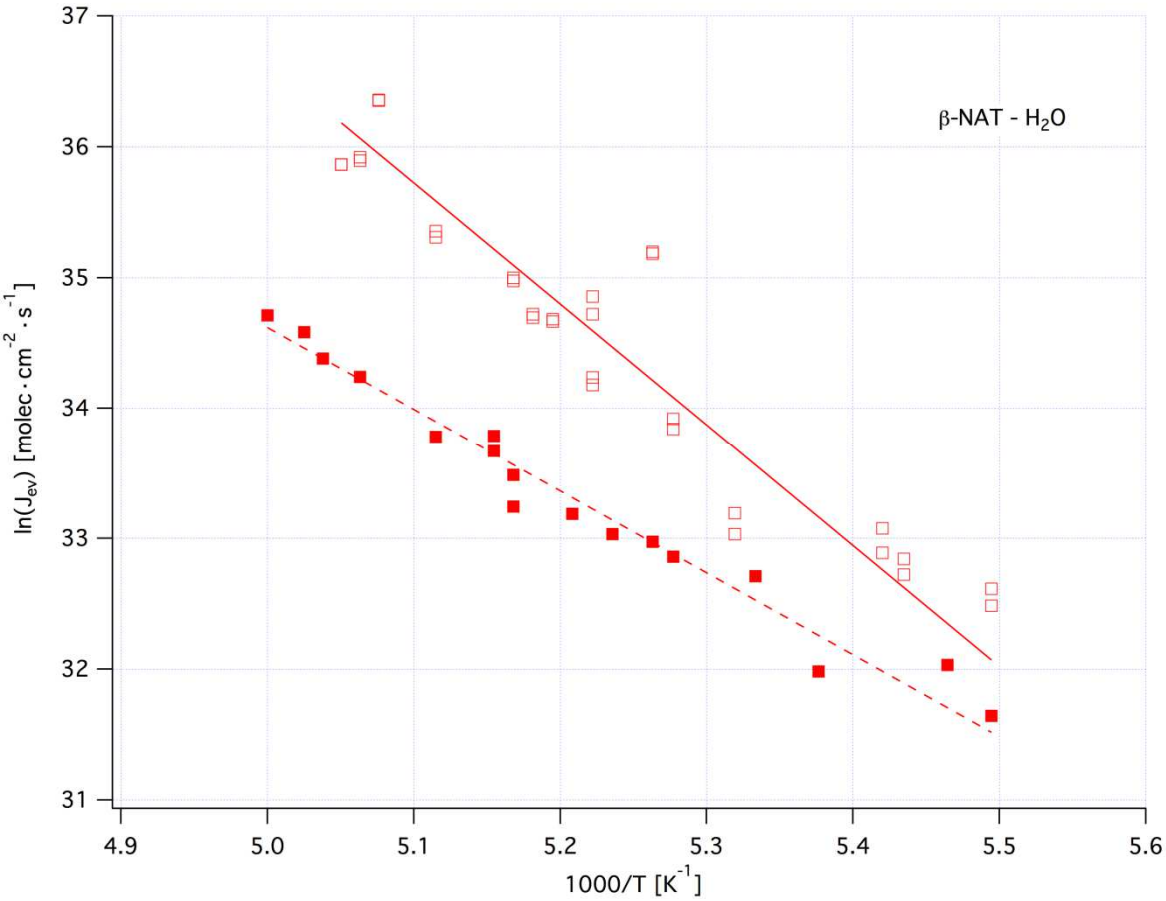

1316

1317 Figure 12: Arrhenius plot of $J_{ev}(H_2O)$ for β-NAT data displayed in Figure 4b. Full and empty
1318 red squares represent results of PV and TO experiments, respectively. The equations for the
1319 linear fits may be found in the text.

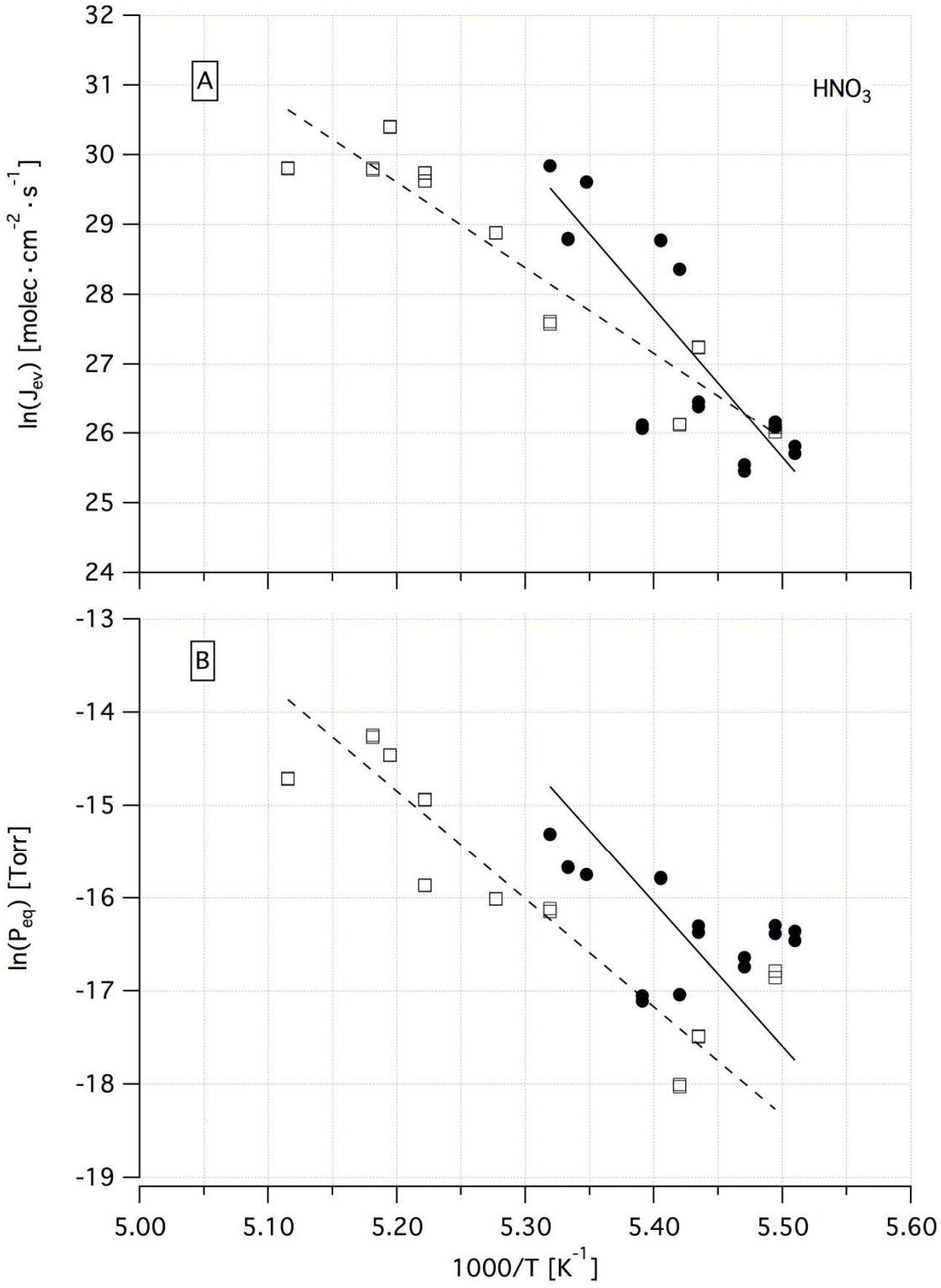

Figure 13: Arrhenius plot of $J_{ev}(HNO_3)$ (A) and van 't Hoff plot of $P_{eq}(HNO_3)$ (B) for α-NAT (Figure 2b and Figure 2c) and β-NAT (Figure 4b and Figure 4c) resulting from TO experiments. Full black circles and empty black squares represent the interaction of HNO_3 with α- and β-NAT films, respectively. The equations for the fitting lines may be found in the text.

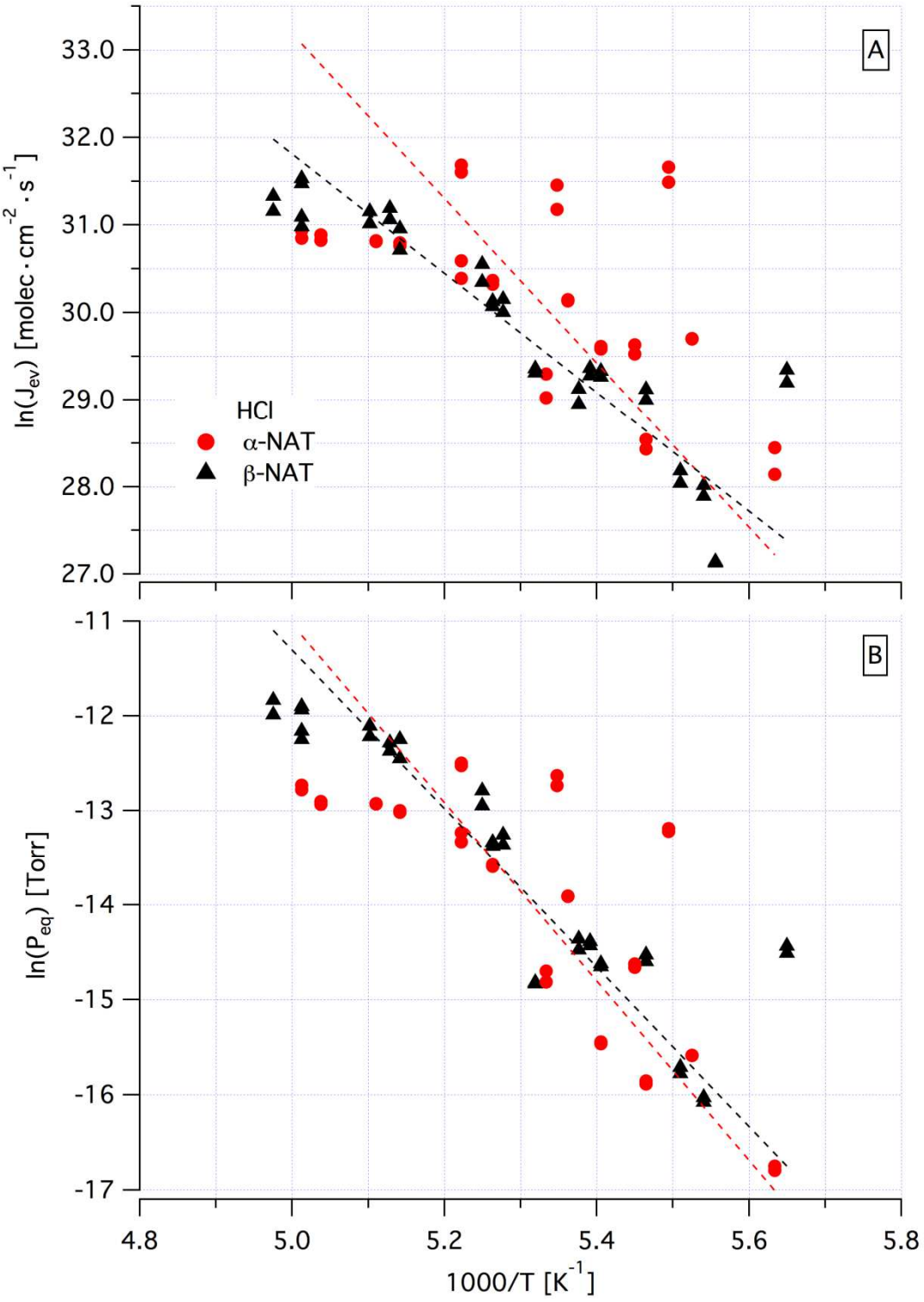

Figure 14: Arrhenius plot of J_{ev}(HCl) (A) and van 't Hoff plot of P_{eq}(HCl) (B) for α-NAT (Figure 8b and Figure 8c) and β-NAT (Figure 9b and Figure 9c) resulting from PV experiments. Full red circles and black triangles represent the interaction of HCl with α- and β-NAT films, respectively. The equations for the fitting lines may be found in the text.